pubs.acs.org/Biomac

Article

# Controlled Release of Drugs from Extracellular Matrix-Derived Peptide-Based Nanovesicles through Tailored Noncovalent Interactions

*Published as part of Biomacromolecules virtual special issue "Peptide Materials".*

Haofu Huang, Jeongmin Hwang, Sudha Anilkumar, and Kristi L. Kiick*

Cite This: *Biomacromolecules* 2024, 25, 2408−2422

Read Online

ACCESS | Metrics & More | Article Recommendations | Supporting Information

**ABSTRACT:** Elastin−collagen nanovesicles (ECnV) have emerged as a promising platform for drug delivery due to their tunable physicochemical properties and biocompatibility. The potential of nine distinct ECnVs to serve as drug-delivery vehicles was investigated in this study, and it was demonstrated that various small-molecule cargo (e.g., dexamethasone, methotrexate, doxorubicin) can be encapsulated in and released from a set of ECnVs, with extents of loading and rates of release dictated by the composition of the elastin domain of the ECnV and the type of cargo. Elastin-like peptides (ELPs) and collagen-like peptides (CLPs) of various compositions were produced; the secondary structure of the corresponding peptides was determined using CD, and the morphology and average hydrodynamic diameter (∼100 nm) of the ECnVs were determined using TEM and DLS. It was observed that hydrophobic drugs exhibited slower release kinetics than hydrophilic drugs, but higher drug loading was achieved for the more hydrophilic Dox. The collagen-binding ability of the ECnVs was demonstrated through a 2D collagen-binding assay, suggesting the potential for longer retention times in collagen-enriched tissues or matrices. Sustained release of drugs for up to 7 days was observed and, taken together with the collagen-binding data, demonstrates the potential of this set of ECnVs as a versatile drug delivery vehicle for longer-term drug release of a variety of cargo. This study provides important insights into the drug delivery potential of ECnVs and offers useful information for future development of ECnV-based drug delivery systems for the treatment of various diseases.

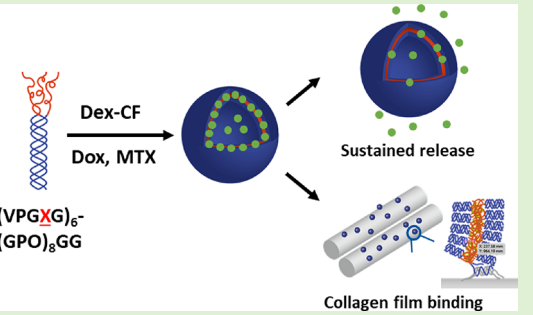


## INTRODUCTION

Nanoparticles (NP) have gained increasing research attention and wide use in various industries, especially as nanomedicines, valued at about $170 billion in 2020 and expected to grow at an annual rate approaching 10% through 2030.[1] In general, nanomedicines comprise NPs with dimensions ranging from 1 to 100 nm,[2] which enables particles to penetrate tissues as well as traverse the cell membrane and also allow them to encapsulate other molecules to aid in their passage through physical barriers.[3,4] A recent prominent example is the lipid-based NP mRNA COVID-19 vaccine,[5−7] although other types of NP carriers such as liposomes,[8] polymersomes,[9] and inorganic NPs[10] have been investigated for decades since the introduction of the first commercially available liposome-based anticancer nanomedicine, DOXIL.[11] Although there are many advantages of NP nanocarriers, some limitations have motivated exploration of new NP formulations,[12] for example, liposomes can show limited physical stability, thus causing burst release of cargo, and polymersomes can exhibit toxicity at high polymer concentrations.[13] Therefore, research has continued on NPs that exhibit high biocompatibility, bioavailability, and stability, including those with their origin from peptides and proteins.[14] Peptide-based NPs have specific benefits, such as engineerable self-assembly that can be tuned by the natural secondary structure of the protein fragments/peptides, a large variety of functional groups provided by different natural and non-natural amino acids, and easily synthesized sequences.[14−17] With the ability to expand their functionality by conjugating peptide-based NPs with other molecules such as fatty acids or polysaccharides, they can also be utilized as biocatalysts or drug delivery carriers.[18−20]

As a target application for NP-based drug delivery, delivery systems that could treat arthritis remain of interest. Post-traumatic osteoarthritis (PTOA) is an insidious consequence of joint injury, which affects more than 3 million new patients

Received: December 10, 2023
Revised: March 18, 2024
Accepted: March 19, 2024
Published: March 28, 2024

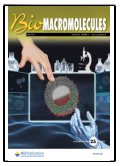







https://doi.org/10.1021/acs.biomac.3c01361
*Biomacromolecules* 2024, 25, 2408−2422

annually in the US,[21,22] and rheumatoid arthritis (RA) is a chronic inflammatory disorder that can also affect joints.[23] They can both cause tremendous pain and are incurable, representing a significant burden on individual patients and on society. Dexamethasone and methotrexate have been used to treat late-stage arthritic inflammation and pain, to provide an inexpensive and easily administered mitigation treatment for PTOA and RA.[23−28] However, clinical implementation suffers from low solubility, which leads to low bioavailability in the physiological environment, and without certain modifications, the off-target effect of drugs can cause severe side effects such as liver damage and gastrointestinal (GI) problems.[23,24] As a solution to the poor targeting and poor bioavailability of antiarthritic drugs to the joint, intra-articular injection has been employed to locally deliver therapeutics to injured joints.[29−31] However, the rapid synovial fluid turnover efficiently clears both small and large molecules from the joints within hours, leading to poor targeting efficiency. To overcome this, reoccurring injection is needed, which requires a high dosage (0.5 mg/kg) that significantly increases cost and off-target effects.[32] Accordingly, a series of drug delivery systems have been developed as mentioned above, among which peptide-based NPs have shown potential to be utilized as the carrier for hydrophobic or hydrophilic drugs owing to their compositional flexibility.[33−38]

Past experimental work from our group introduced elastin- and collagen-peptide-based nanovesicles (Elastin−Collagen nano-Vesicles (ECnVs)), which have demonstrated the ability to encapsulate hydrophobic model molecules.[39,40] Composed of two different thermally responsive peptides−elastin-like-peptides (ELP) and collagen-like-peptides (CLP), ECnVs show chemical and physical properties that are derived synergistically from both the ELP and CLP domains. ELP comprises the pentapeptide repeats of $(VPGXG)_n$, where V, P, and G are valine, proline, and glycine, and X can be any amino acid except proline.[41] ELPs of higher molecular masses are known to undergo a lower critical solution temperature (LCST)-like phase transition in aqueous solutions where the ELP is soluble below the transition temperature, $T_t$, and forms protein-rich coacervate phases above the $T_t$, which can be manipulated by changing solution conditions such as the concentration, pH, guest residues.[42−44] Shorter ELPs (fewer than 10 repeats of the VPGXG pentapeptide) have been less studied than the longer ELPs (tens and hundreds of repeats of the pentapeptide) because the shorter ELPs generally exhibit high $T_t$ (above 100 °C). Nonetheless, owing to their thermoresponsiveness and scalable solid-phase manufacturing, short ELPs could be valuable candidates for stimuli-responsive drug nanocarriers if they can be modified to exhibit $T_t$ values near physiological temperatures.

Our previous work has demonstrated that such manipulation is possible by the covalent conjugation of ELPs with CLPs. The CLPs comprise the tripeptide repeats of $(G\text{-}X\text{-}Y)_n$, where $n$ is generally between 6 and 10 and where X and Y can be either proline or hydroxyproline.[45] CLPs are known to form triple helices under their "melting" temperature $T_m$ and to unfold into random-coil monomers above the $T_m$. Through judicious design, the thermoresponsiveness of the ECnVs can be manipulated individually through slight changes in the ELP and the CLP sequences,[46−48] which provides significant opportunities for ECnVs in applications that require different stimuli-triggered temperatures. The conjugation of CLPs to short ELPs of appropriate composition and length yields ELP-CLP conjugates that can self-assemble into nanoparticles with $T_t$ near physiological temperature presumably because the CLP triple helix formation increases the local concentration of the ELP, which leads to a significant decrease in $T_t$.[40] We have further shown that the ECnVs, once assembled, are highly stable structures. ECnVs remain intact for at least 7 days of dialysis at low ECnV concentration[49] and retain their vesicular structure after centrifugation and resuspension and even after one year of ambient storage in aqueous solution (data not shown). Furthermore, fluorophore-labeled ECnVs are able to survive several steps of dehydration through graded ethanol, as well as the xylene clearing and molten paraffin infiltration necessary for histological processing.[50]

Previous studies conducted by Yu and co-workers have shown that unfolded, single-strand CLPs have a strong propensity to target denatured collagen via highly efficient and specific triple helix hybridization.[51] A previous study conducted by Luo et al. showed that ECnVs are also competent to bind to collagen films, which indicates the possibility of employing ECnVs as collagen-targeting drug carriers, especially for diseases associated with high collagen remodeling such as PTOA, RA, Marfan syndrome, cancer, and osteogenesis imperfecta.[39] Hydrophobic drug molecules can be localized in ECnVs, presumably through interactions with the ELP hydrophobic domain.[35] Given the types of interactions that dictate assembly of ECnVs and their interaction with collagen-containing tissues, we have explored the types of interactions that can modify the interactions of ELPs and thus the assembly of ECnVs.[48,52]

Past experimental work from the Kiick group and simulation studies from the Jayaraman group have shown the importance of the fourth guest residue, X, in the ELP sequence to the intra- and intermolecular interactions within the ECnVs.[48,52] For example, when switching the guest residue X between phenylalanine (F), tyrosine (Y), and tryptophan (W), the $T_t$ and morphologies of the ECnVs changed significantly due to differences in intra- and intermolecular interactions such as hydrophobic interactions, pi-pi stacking, and hydrogen bonding. When it comes to the encapsulation of drug molecules, due to the amphiphilic nature of the ECnVs, the hydrophobic molecules are likely sequestered in the hydrophobic ELP domain. Because studies have shown that strong noncovalent interactions between drug molecules and nanocarriers can lead to a high encapsulation rate and sustained release,[53] we postulated that the guest residue in the ELP domain should play a significant part in the drug encapsulation process. The potential for these ELP-based nanocarriers, with different guest residues, as drug nanocarriers was thus investigated.

There are a variety of different drugs that would be of interest for encapsulation in ECnVs and subsequent localization to diseased ECM. Dexamethasone, as mentioned above, is a hydrophobic, traditional symptom-managing drug for mitigation of PTOA, although limited by its low bioavailability. Methotrexate is an immunosuppressant drug that can reduce inflammation by suppressing the immune system although limited by the severe side effects when taken orally, and doxorubicin, a traditional anticancer drug, has seen widespread use, yet its dosage is often constrained due to the elevated risk of off-target effects. Other therapeutics such as nucleic acids, peptides, and proteins can also benefit from sequestration in drug delivery platforms (liposomal, polypeptide).[54−56] Therefore, peptide-based nanocarriers based on ECnVs that improve


https://doi.org/10.1021/acs.biomac.3c01361
Biomacromolecules 2024, 25, 2408−2422

bioavailability and limit off-target effects could have value in the delivery of these cargoes, through demonstrated improved retention via extracellular targeting, electrostatic interactions, and/or tissue affinity to extracellular matrix (ECM).[50] Previous studies have been conducted on Dex incorporated in PLGA microsphere/PLGA microsphere-containing hydrogels,[57,58] with delivery sustained from the microspheres. Hwang et al.[49] have also compared the release of vancomycin (Van) from Van-loaded ECnVs incorporated into hydrogels with Van-loaded liposomes (DSPE-PEG)-incorporated into hydrogels. Van-loaded ECnV-based hydrogels exhibit increased retention and slower release, suggesting that the reported ECnV approaches have advantages relative to traditional liposome-based drug-delivery vehicles.

In this work, we successfully encapsulated dexamethasone fluorescein (Dex-CF), doxorubicin hydrochloride (denoted as Dox), and methotrexate (MTX) in each of three different classes of ECnVs and obtained 7-day sustained release profiles that also exhibit thermally stimulated release. The impact, on cargo loading and release, of the noncovalent interactions between different drug molecules and the various ECnVs was evaluated. Furthermore, the physical properties of the drug-encapsulated ECnVs were characterized via dynamic light scattering, transmission electronic microscopy, and fluorescence measurements. We also performed collagen-binding assays to confirm the possible retention of the various ECnVs and collagen films. These studies suggest that ECnV carriers exhibit sufficient versatility for manipulation of drug-loading efficiency for different drug classes and extended rates and/or thermally triggered drug release postinjection. This study is the first to compare the drug loading efficiency of ECnVs with different ELP guest residues and suggests that the ECnVs could be promising candidates as collagen-targeting drug nanocarriers.

## EXPERIMENT AND MATERIALS

**Materials.** All Fmoc-protected amino acids (glycine, proline, hydroxyproline, valine, phenylalanine, tyrosine, cysteine, and Fmoc-propargyl glycine), 4-azidobutanoic acid, Oxyma Pure, and hexafluorophosphate (HBTU) for solid-phase peptide synthesis were purchased from Chempep (Wellington, FL). *N*,*N*′-Diisopropyl carbodiimide (DIC) and *N*,*N*-diisopropylethylamine (DIPEA) were purchased from Sigma-Aldrich (St. Louis, MO). HPLC-grade acetonitrile, dimethylformamide (DMF), and ethyl ether were purchased from Fisher Scientific (Fairlawn, NJ). Triisopropylsilane (TIPS), diisopropylethylamine (DIPEA), trifluoroacetic acid (TFA), Cu(II) sulfate, (+)-sodium L-ascorbate, tris(benzyl triazolyl methyl)-amine (THPTA), and dehydrated DMSO used in cleavage and CuAAc click reaction were purchased from Sigma-Aldrich (St. Louis, MO). Doxorubicin hydrochloride (Dox), dexamethasone fluorescein (Dex-CF), *N*-hydroxysulfosuccinimide (sulfo-NHS), 1-ethyl-3-(3-dimethyl aminopropyl) carbodiimide (EDC), tris(2-carboxyethyl) phosphine hydrochloride (TCEP), Alexa Fluor 555 cadaverine (AF555), and Cy3 maleimide for drug delivery and particle labeling were purchased from Thermo Fisher Scientific (Waltham, MA). AZDye 350 NHS ester and AZDye 405 NHS ester were purchased at Fluoroprobes, LLC (Scottsdale, AZ). Corning collagen I and rat and bovine serum albumin (BSA) for the collagen-binding assays were purchased from Fisher Scientific (Fairlawn, NJ).

**Synthesis of Collagen-like Peptides and Elastin-like Peptides.** The collagen-like peptide (CLP) with the sequence: $(GPO)_8GG$ with an amidated C-terminus (denoted as $G_8GG$ or $G_8$), $(GPO)_8GG$-COOH with a carboxylic acid-functionalized C-terminus (denoted as $G_8GG$-COOH), $(GPO)_8GC$ (denoted as $G_8GC$), and elastin-like-peptides (ELP) with sequences: $(VPGFG)_6G'$ (denoted as $F_6$), $(VPGYG)_6G'$ (denoted as $Y_6$), $(VPGWG)_6G'$ (denoted as $W_6$) ($G'$: propargyl glycine) were synthesized via traditional solid-phase peptide synthesis using a Liberty Blue Automated Microwave Peptide Synthesizer (CEM Corporation, Charlotte, NC). The additional GG group of the CLP sequence was added for ease of experimental synthesis as it inhibits potential side reactions at the C-terminus of the CLP triple helix. The general synthesis scale was 0.25 mmol using a 0.19 mmol/g low-loading Rink Amide ProTide Resin (CEM corp, Matthews, NC). The CLP sequence $G_8$OH was synthesized at a 0.25 mmol scale on a 0.49 mmol/g glycine-preloaded Wang resin. Double coupling and single deprotection were conducted on both CLP and ELP syntheses. DIC and Oxyma were used for activation of carboxylic acids, and 20% v/v piperidine was used for the deprotection of the Fmoc group. The single coupling cycle was 125 s (70 °C for 15 s and 90 °C for 110 s). 4-Azidobutanoic acid was manually coupled to the N-terminus of the CLP when on the resin using HBTU/DIPEA for carboxylic acid activation. A 10:1 molar ratio of 4-azidobutanoic acid to resin was used for the conjugation. Cleavage of the peptides from the resin was conducted in 93:4.5:2.5 (v:v:v) TFA/TIPS/$H_2O$ for 2 h at room temperature, and the cleaved peptide was precipitated in cold anhydrous ethyl ether. Crude peptides were purified via reverse-phase HPLC ($C_{18}$ column) at room temperature. The mobile phase comprised gradients of degassed deionized water with 0.1% TFA and acetonitrile with 0.1% TFA, at a flow rate of 30 mL/min. Then, the peptide was detected by a UV detector at 214 nm. Fractions with products were collected and lyophilized. The molecular weight of the peptides was confirmed via electrospray ionization mass spectrometry (ESI-MS Waters Xevo TQ-GC Mass Spectrometry System, Milford, MA), and the purity of the peptide was confirmed via reverse-phase UPLC (Waters, Milford, MA) (Figures S1−S6).

**Synthesis of the ELP-*b*-CLP Conjugates.** The CLP sequences were conjugated to various ELPs via the copper(I)-catalyzed azide−alkyne cycloaddition (CuAAC) "click" reaction. Stock solutions of 350 mM THPTA, 200 mM Cu(II) sulfate, and 2 M (+)-sodium L-ascorbate were prepared fresh in HPLC-grade water at room temperature. CLP (6 μmol) and ELP (3 μmol) were weighed and predissolved in a nitrogen-purged glass vial containing 370 μL of HPLC-grade water. (+)-Sodium L-ascorbate (200 μL) and DMSO (300 μL) were then added to the same vial. THPTA (100 μL) and Cu(II) sulfate (30 μL) were premixed and then added to the previous solution making the final concentration of each reagent: 35 mM THPTA, 400 mM (+)-sodium L-ascorbate, and 6 mM Cu(II) sulfate in a 70% water (v/v) and 30% DMSO (v/v) solution. The mixture was stirred for 1 h above the melting temperature of $G_8GG$ at 70 °C (which was determined by circular dichroism measurements). The CLP and the ELP were connected via the formation of the triazole group upon reaction of the alkyne group on the ELP and the azide group on the CLP. Reverse-phase HPLC purification was performed immediately after the reaction by injecting all solutions into the $C_{18}$ column. The mobile phase comprised gradients of degassed deionized water with 0.1% TFA and acetonitrile with 0.1% TFA, at a flow rate of 30 mL/min. The column was heated to above 65 °C to unfold the ELP-CLP trimer, and the eluted peptide was detected by a UV detector at 214 nm. Fractions with products were collected and lyophilized. The molecular weight of the peptides was confirmed via electrospray ionization mass spectrometry (ESI-MS Waters Xevo TQ-GC Mass Spectrometry System, Milford, MA), and the purity of the conjugates was confirmed by reverse-phase UPLC ($C_{18}$ column). Results are shown in Figures S7−S12.

**Self-Assembly of ELP-CLP Conjugates and Drug Encapsulation.** Powder samples (1.5 mg) of each of the purified ELP-CLPs were weighed and separated equally into three glass vials (0.5 mg in each vial) for each sequence. One milliliter of HPLC-grade water was added respectively to the three vials to dissolve the peptides and yield a final concentration of 0.5 mg/mL. Because the transition temperature ($T_t$) of the ELP domain changes as a function of concentration, even in the short ELP sequences,[59] the concentration of the ELP and the ECnV was kept constant for data accuracy. The three vials of solution were incubated in an oven and heated above their $T_m$ (determined via CD measurements, shown in Figures 2 and S13) at 80 °C for 2 h to completely dissociate the ELP-CLP. Twenty


https://doi.org/10.1021/acs.biomac.3c01361
Biomacromolecules 2024, 25, 2408−2422

microliters of predissolved Dox, Dex-CF, or MTX (25 mg/mL) were added respectively into each of the three vials after the heating process to yield a 1:1 weight ratio of the ELP-CLP to the candidate drug. The three vials of solution were removed from the oven and incubated at room temperature overnight before other measurements. The drug-containing solutions from the three vials were transferred into three low-protein-binding collection tubes (Thermo Fisher Scientific, US) and centrifuged in an Eppendorf microcentrifuge 5424 (Eppendorf, Enfield, CT) at 15,000 rpm for 10 min to pellet the drug-loaded ECnVs. The supernatant was removed before adding another 1 mL of HPLC-grade water at room temperature. Another two cycles of centrifugation were conducted afterward to remove any excess drug. Particle pellets were resuspended in 1 mL of HPLC-grade water and sonicated until no visible pellets remained in the solutions after the final centrifugation, to avoid particle aggregation. 10× PBS (111 $\mu$L) was added to yield a final buffer composition of 1× PBS prior to taking any other measurements. The hydrodynamic diameter and morphology of the ECnVs were confirmed through dynamic light scattering (DLS) and transmission electron microscopy (TEM) measurements.

**Circular Dichroism (CD) Spectroscopy.** Circular dichroic spectroscopy (Jasco 1000 circular dichroism spectropolarimeter, Jasco Inc., Easton, MD) was conducted for the characterization of the secondary structure of the CLP domain. CLP and ELP−CLP conjugates were dissolved at a concentration of 100 $\mu$M in 1× PBS (10 mM, pH 7.4, 137 mM NaCl, and 2.7 mM KCl) and incubated at 4 °C overnight prior to measurement. The CD spectra were recorded using quartz cells with a 0.1 cm optical path length. Full wavelength scans were collected to study the conformation of the peptide domain at 4 °C. The scanning rate was 50 mm/min, with a response time of 4 s. The wavelength scans were obtained from 200 to 250 nm and were recorded every 1 nm. To measure the melting temperature of the CLP domain, variable temperature experiments were conducted at the maximum wavelength in each ELP−CLP conjugate (e.g., 224 nm) with a 6 °C/h heating rate from 4 to 80 °C. Boltzmann fitting of the melting curve was conducted, and the corresponding temperature with the highest first derivative was defined as the melting temperature ($T_m$).

**Dynamic Light Scattering (DLS).** The solutions of ECnVs were transferred into Hellma quartz cuvettes (1 × 1 cm light path) after formation of the ECnVs. Analysis of particle sizes with and without drugs was conducted via dynamic light scattering (DLS) on a Zetasizer Nano series (Nano ZS, Malvern Instruments, U.K.) at a scattering angle of 173°. Solutions were incubated at 37 °C for 5 min before conducting measurements (employing the automatic measure position and attenuator) were selected. The number distribution was reported to highlight the most dominant hydrodynamic diameter ($D_h$) that the ECnVs exhibit at a specific temperature. The transition temperature ($T_t$) of a given ELP-CLP conjugate was obtained by measurement of the average hydrodynamic diameter of nanoparticles at temperatures from 4 to 80 °C with a temperature interval of 3 °C. Samples were incubated at each temperature for 5 min before measurement. Each data point in the DLS results was calculated from the average of three different measurements, and the error was calculated from their standard deviation. The first derivative of the temperature curve was calculated, and the corresponding temperature with the highest value was labeled as the $T_t$ to be consistent with previous reports.[48]

**Transmission Electron Microscopy (TEM).** TEM samples were prepared on carbon-coated ultrathin copper grids (Electron Microscopy Science, Hatfield, PA). Grids, pipet, pipet tips, and the ECnV solution in deionized water (1 mg/mL; self-assembled as described in the previous section) were incubated in an isothermal oven at 37 °C for at least 1 h before preparing the TEM grids. Five microliters of sample solution was dropped on the grid and blotted after 120 s. For staining, 1% phosphotungstic acid (PTA; pH adjusted to 7.0 using 2 M NaOH) as a negative stain was used. A total of 3 $\mu$L of the PTA solution was dropped on the grid and blotted after 10 s at 37 °C. The grid was incubated in the oven at 37 °C for at least 1 h (until dried) and stored at room temperature overnight before imaging. TEM images were collected on a Tecnai G2 at a 120 keV accelerating voltage and on a Talos F200C at a 200 keV accelerating voltage.

**Release of Dex-CF/Dox/MTX from ECnVs.** The release profiles of encapsulated Dex-CF, Dox, or MTX from the ECnVs were determined at physiological temperature (37 °C). The drug-loaded ECnV solutions (0.5 mL) at 0.5 mg/mL in 1× PBS was carefully injected into a 0.5 mL Slide-A-Lyzer MINI Dialysis Device (MWCO 10 kDa, Thermo Fisher Scientific Inc., Waltham, MA) and dialyzed against the membrane in 14 mL of 1× PBS solutions for 7 days at 37 °C. We note that the physical properties of the ECnVs, such as morphology and dimensions, are responsive to differences in buffer pH (manuscript in preparation); thus, all the release and imaging was conducted with 1× PBS as buffer to permit valid comparisons between peptide sequences. At predetermined time points, 3 mL of the dialysis buffer were collected and replenished with 3 mL fresh 1× PBS. The release of the Dex-CF/Dox was monitored by measuring the fluorescence intensity of the collected sample on a Spectramax i3x microplate reader (Waltham, MA, U.S.A.), with excitation/emission wavelengths of 485/535 nm for Dex-CF and 470/595 nm for Dox at room temperature. The release of the MTX was monitored by measuring the UV absorbance of the collected sample with a NanoDrop 2000 spectrophotometer at 304 nm at room temperature. On day 7, after sample collection, the ECnV solutions were mixed with the PBS dialysis solutions and incubated at 80 °C for at least 1 h to completely dissociate the ECnVs. Drug concentrations after liberation from the ECnVs upon their dissociation at elevated temperatures were measured on a Spectramax i3x microplate reader. The cumulative amount of total released drug was calculated and used as the total amount of initially encapsulated drug. The reported data represent an average of three synthetic experimental repeats.

The encapsulation efficiency (EE) and loading capacity (LC) were determined based on the unencapsulated drug molecules in the supernatant. The EE of all three drug molecules was calculated using the following formula:

$$\mathrm{EE} = \frac{M_{\text{drug loaded in ECnVs}}}{M_{\text{initial drug}}} \times 100 \tag{1}$$

where $M_{\text{drug loaded in ECnVs}}$ is the mass of drug that has been loaded in the ECnVs and $M_{\text{initial drug}}$ is the initial mass of drug added to the ELP-CLP solution for encapsulation.

The LC of drug in the ECnVs was calculated using the following formula:

$$\mathrm{LC} = \frac{M_{\text{drug loaded in ECnVs}}}{M_{\text{ECnVs}}} \times 100 \tag{2}$$

where $M_{\text{drug loaded in ECnVS}}$ is the mass of drug that has been loaded in the ECnVs and $M_{\text{ECnVs}}$ is the mass of the ECnVs.

After collecting the release solution at the indicated time points, the concentration of the drug in the solution was determined using a standard curve. The cumulative percentage release of drug molecules per sample was calculated using the following equation:

$$p = \frac{V_e \sum_1^{n-1} C_i + V_0 C_n}{M_{\text{drug loaded}}} \times 100\% \tag{3}$$

where $V_e$ represents the volume of each sample that was collected at each time point, $C_i$ represents the concentration of drug in the $i$th sample, $V_0$ represents the total volume of the release media, $C_n$ represents the concentration of drug in the $n$th sample, and $M_{\text{drug loaded}}$ represents the amount of drug that has been encapsulated in the ECnVs.[60]

**Fluorescent Labeling of the ECnVs and Dex-CF/Dox Encapsulation for Fluorescence Resonance Energy Transfer (FRET) Assay.** The ELP domain of $F_6$-$G_8$GG (and $Y_6$-$G_8$GG and $W_6$-$G_8$GG) was labeled with an AZDye 350 or AZDye 405) via NHS ester/amine reaction. $F_6$-$G_8$GG (0.1 mg) (and $Y_6$-$G_8$GG and $W_6$-$G_8$GG) was weighed into a glass vial, and 75 $\mu$L of 1× PBS (10 mM, pH 7.4, 137 mM NaCl, and 2.7 mM KCl) was used to dissolve the


https://doi.org/10.1021/acs.biomac.3c01361
Biomacromolecules 2024, 25, 2408−2422

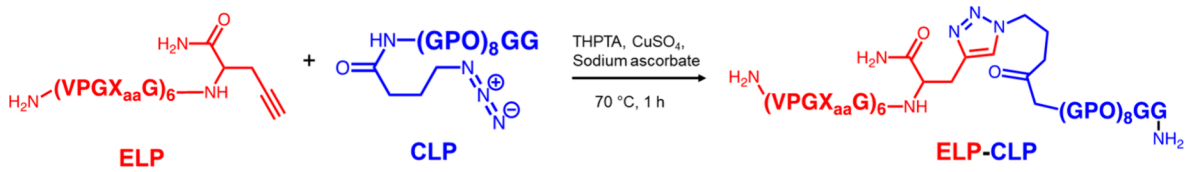


**Figure 1.** Reaction scheme for production of the ELP-CLP conjugates via copper(I)-mediated azide−alkyne cycloaddition reaction.

powder. The solutions were incubated at 80 °C for at least 1 h to disassociate the ECnVs. The solution of the dissociated ECnVs was transferred into an Eppendorf ThermoMixer after adding 25 μL of predissolved AZDye 350 NHS ester (or AZDye 405 NHS ester) (10 mg/mL) and mixed at 80 °C for 1 h. Another 0.9 mg of $F_6$-$G_8$GG ($W_6$-$G_8$GG and $Y_6$-$G_8$GG) was weighed and dissolved in 0.9 mL of 1× PBS solution and was then heated at 80 °C for 2 h. These two solutions were then mixed and transferred into a low-protein-binding tube at 80 °C. Forty microliters of Dex-CF (or Dox) stock solution at 25 mg/mL was added into the tube. The solution was protected from light exposure by wrapping in Al foil and stored overnight at 37 °C to permit assembly of the ECnVs, which was followed by centrifugation at 15,000 rpm to pellet down the ECnVs. The supernatant was carefully drawn out via pipet to remove the unencapsulated drug and unreacted dyes, and fresh PBS was added followed by repeat centrifugation and supernatant removal. The rinsing process was repeated three times, and elimination of the unreacted dye was confirmed via measuring the fluorescence intensity of the collected supernatant. The ECnV solutions were vortexed after resuspending the ECnVs in 1 mL of HPLC-grade water, which prevented the aggregation of the ECnVs and yielded a final ECnV concentration of 1 mg/mL.

**FRET Assays.** FRET experiments for Dex-CF encapsulated (and Dox encapsulated) $F_6$-$G_8$GG, $Y_6$-$G_8$GG, and $W_6$-$G_8$GG were conducted on a Spectramax i3x microplate reader after the encapsulation and labeling of the ELP domain with AZDye 350 (AZDye 405) as mentioned above. For FRET on Dex-CF encapsulated ECnVs, particle solutions were excited at a wavelength of 350 nm and emission signals were collected from 400 to 550 nm. For FRET experiments on Dox-encapsulated ECnVs, particle solutions were excited at a wavelength of 405 nm and emission signals were collected from 450 to 700 nm. Signals were collected with a microplate reader and replotted in Microsoft Excel.

**Fluorescent Labeling of the ECnVs for Collagen Binding.** The CLP domain of $F_6$-$G_8$GC ECnV was labeled via thiol-maleimide reaction, while the CLP domains of $Y_6$-$G_8$GG ECnV and $W_6$-$G_8$GG ECnV were labeled via EDC/sulfo-NHS reaction.

*$F_6$-$G_8$GC Thiol Labeling with Cy3 Maleimide.* $F_6$-$G_8$GG (1.8 mg), $F_6$-$G_8$GC (0.2 mg), and TCEP (0.12 mg) were weighed and mixed in a glass vial. 1× PBS (386 μL) was used to dissolve the powder. (TCEP was added to prevent oxidation of the Cys in $F_6$-$G_8$GC.) The solution was then oven-incubated at 80 °C for at least 1 h to disassociate the ELP-CLP trimers. The solution was removed from the oven and left at room temperature overnight to allow the ECnVs to self-assemble. The solution of self-assembled ECnVs was transferred to an Eppendorf ThermoMixer after adding 14 μL of predissolved Cy3 maleimide solution (20 mg/mL) and mixed at 37 °C for 2 h. The particle solution was then transferred into a low-protein-binding tube and centrifuged at 15,000 rpm, 25 °C for 10 min to pellet the ECnVs. The supernatant was carefully drawn out and discarded before resuspending the ECnVs in 1 mL of 1× PBS, to yield a stock solution of the labeled ECnVs at a concentration of 2 mg/mL. DLS and TEM were performed as described above at room temperature to confirm that the ECnVs remained intact and to verify their morphology. Samples were diluted to desired concentrations before conducting other experiments (0.5 mg/mL for TEM measurements, 1 mg/mL for DLS measurements, and 0.1 mg/mL for 2D collagen-binding essays).

*$W_6$-$G_8$GG and $Y_6$-$G_8$GG Labeling with AF555-Cadaverine.* $W_6$-$G_8$GG (1.8 mg) (or $Y_6$-$G_8$GG) and $W_6$-$G_8$GG-COOH (0.2 mg) ($Y_6$-$G_8$GG-COOH) were weighed and mixed in a glass vial. HPLC-grade water (150 μL) was used to dissolve the powder. Incubation (80 °C) for at least 1 h was conducted before overnight room-temperature incubation. Stock solutions of 52 mM EDC and 46 mM sulfo-NHS were prepared fresh in HPLC-grade water before the reaction. EDC (5.85 μL) and sulfo-NHS (5.8 μL) were mixed into the particle solution while shaking. The solution of self-assembled ECnVs, with 25 μL of predissolved AF555 cadaverine (20 mg/mL), was mixed in an Eppendorf ThermoMixer at 37 °C for 1 h. The particle solution was then transferred into a low-protein-binding tube, and centrifugation was conducted to pellet the ECnVs. The supernatant was carefully removed and discarded. The particle solution was vortexed after resuspending the ECnVs in 1 mL of HPLC-grade water, which prevented the aggregation of the ECnVs and yielded a final concentration of 2 mg/mL. DLS and TEM were performed at room temperature as described above to determine that the ECnVs remained intact and that their morphology remained unchanged. Particle solutions were transferred into a dts1070 folded capillary cell (Malvern Panalytical Inc., Westborough, MA), and zeta-potential measurement was performed on a Zetasizer Nano series to confirm the change in surface potential after modification. Samples were diluted to desired concentrations prior to conducting other experiments (0.5 mg/mL for TEM measurements, 1 mg/mL for DLS measurements, and 0.1 mg/mL for 2D collagen-binding essays).

**Collagen-Binding Assay.** Corning collagen type I from rat tail was used for collagen coating onto the plate wells. Collagen liquid (3.3 mg/mL) was diluted in 1× PBS to 0.2 mg/mL at room temperature to make a fresh collagen stock solution. Nunc MaxiSorp flat-bottom high protein binding plate (96-well) was used. The stock solution (100 μL) was added into each predetermined well before settling the entire plate on a benchtop shaker (220 rpm) at room temperature for overnight coating. The leftover collagen solution was discarded the next day, and 200 μL of 1× PBS was used for each well to wash the unbonded collagen 3 times. 5% BSA (w/w) was made fresh in 1× PBS. The BSA stock solution (100 μL) was added to each well and incubated in a 37 °C shaker for 30 min to avoid nonspecific binding with the wells. The excessive BSA solution was discarded, and wells were washed three times with 200 μL 1× PBS each. The labeled ELP-CLP stock solutions were diluted to 0.1 mg/mL in HPLC-grade water and divided into three groups: heated (70 °C for $W_6$-$G_8$, 60 °C for $F_6$-$G_8$ and $Y_6$-$G_8$), 55 °C, and 37 °C. Solutions in the heated group were incubated at their melting temperature for 30 min, (predetermined via CD measurements), the 55 °C groups were incubated at 55 °C for 30 min, and the 37 °C groups were incubated at 37 °C for 30 min. Solutions (50 μL) in both groups were added into the predetermined wells, and the initial amount of labeled ECnVs was determined by measuring the fluorescence intensity of the sample under a Spectramax i3x microplate reader (Waltham, MA, U.S.A.), with excitation/emission wavelengths of 554/568 nm for the Cy3 label and 553/568 nm for the AF 555 label. The plate was then incubated in a 37 °C shaker overnight. The incubation solutions were discarded after the overnight incubation, and washes (200 μL of 1× PBS at 37 °C for 10 s) were conducted thrice to remove unbound ECnVs. 1× PBS (50 μL) was added before measuring the fluorescence intensity. The percentage of binding was subsequently quantified by comparing the residual intensity with the initial intensity values.

## RESULTS AND DISCUSSION

**Synthesis of the ELP-CLP Conjugates.** The ELP-CLP conjugates were produced via copper(I)-mediated azide−


https://doi.org/10.1021/acs.biomac.3c01361
Biomacromolecules 2024, 25, 2408−2422

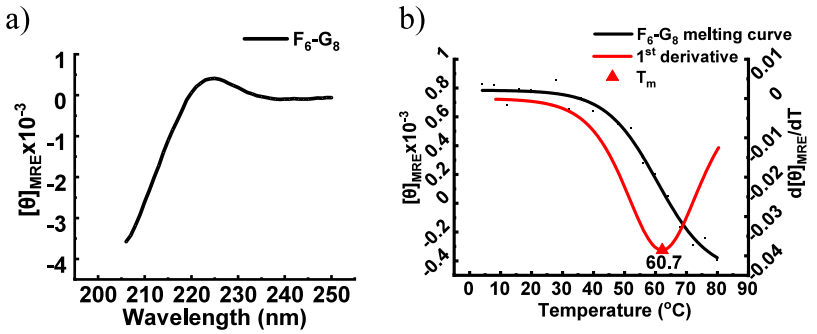


**Figure 2.** Representative full wavelength scan and thermal unfolding profile for ECnVs (with encapsulated drug) obtained from circular dichroism measurement. (a) Full wavelength scan for Dex-CF/$F_6$-$G_8$; (b) thermal unfolding profile for Dex-CF/$F_6$-$G_8$ ($n$ = 3).

**Table 1. Thermal Melting Temperature ($T_m$) of CLPs, from CD Measurements of Drug-Encapsulated ECnVs ($n$ = 3)**

| ECnVs | free | Dex-CF | Dox | MTX |
|---|---|---|---|---|
| $F_6$-$G_8$ | 57.5 ± 1.0 °C | 59.6 ± 0.8 °C | 58.3 ± 0.4 °C | 58.2 ± 1.0 °C |
| $Y_6$-$G_8$ | 59.4 ± 0.7 °C | 59.2 ± 0.9 °C | 58.9 ± 0.7 °C | 60.5 ± 0.8 °C |
| $W_6$-$G_8$ | 67.7 ± 1.2 °C | 70.9 ± 0.5 °C | 68.2 ± 2.1 °C | 68.2 ± 1.0 °C |

alkyne cycloaddition reactions in which the ELP sequences ($Y_6$, $W_6$, or $F_6$) were conjugated with CLP domains comprising $G_8$ sequences (Figure 1). C-terminally alkyne-functionalized ELP domains and N-terminally azide-functionalized CLP domains were synthesized via solid-phase peptide synthesis (SPPS) methods and purified via reverse-phase HPLC with a purity greater than 95% (Figures S1−S6). Then, ELPs were conjugated to the CLPs via copper(I)-catalyzed azide−alkyne cycloaddition. The conjugation reaction was conducted at 70 °C for 1 h in water/DMSO (7:3) solutions. All bioconjugates were purified via HPLC, with a column heated above the CLP triple helix unfolding temperature to avoid triple helix formation on the column. After purification via reverse-phase HPLC, peptides with purity greater than 95% were obtained. Electrospray ionization mass spectrometry (ESI-MS) was used to verify the purity and expected molecular masses of the peptides and ELP-CLP conjugates (Figures S7−S12).

**Thermal Stability of the ECnVs.** All ECnVs of the reported compositions form vesicle-like structures at low temperatures owing to the low $T_t$ values of the ELPs comprising the ECnVs in this study. $F_6$-$G_8$ ($T_t$ ∼ 21 °C) was reported previously by our group, $Y_6$-$G_8$ ($T_t$ < 4 °C) was measured via DLS (Figure S14). Owing to the hydrophobic nature of W relative to Y, $W_6$-$G_8$ also exhibits a $T_t$ of < 4 °C. The measurement of the $T_t$ values for the ECnVs with encapsulated drugs was not possible since the $T_t$ of those two sequences ($Y_6$-$G_8$ & $W_6$-$G_8$) are already below 4 °C; therefore, any quantitative changes in the $T_t$ as a result of the increase in the interactions between the ECnVs and the drug molecules could not be monitored under accessible experimental conditions.

Circular dichroism (CD) measurements were conducted to study the change of the secondary structures within the CLP domain of the ECnVs after drug encapsulation and to investigate if there were any corresponding changes in the thermal stability of the ECnVs. The representative full wavelength scan of the Dex-CF/$F_6$-$G_8$ at 4 °C is shown in Figure 2a, where a maximum molar residue ellipticity was observed at 224 nm, indicating a formation of collagen triple helix. Figure 2b shows the representative thermal unfolding profile of the Dex-CF/$F_6$-$G_8$, where the black curve shows the unfolding curve of the CLP triple helix and the red curve is the first derivative of the unfolding curve, from which the unfolding temperature ($T_m$) of the conjugate was determined. (CD data for the rest of the sequences are shown in Figure S13). By comparing the unfolding profile with the non-encapsulated ECnVs (Figure S13), all three sequences with Dex-CF, Dox, and MTX encapsulation exhibit similar $T_m$ (Table 1) except $F_6$-$G_8$/Dex-CF (2.1 °C increase), $W_6$-$G_8$/Dex-CF (3.3 °C increase), and $Y_6$-$G_8$/MTX (1.1 °C increase). These results suggest that the presence of the hydrophobic molecule (Dex-CF) stabilized the unfolding of the CLP domain by stabilizing the association of the ELP domain as described previously,[18] while possible H-bonding interactions between MTX and the CLP domain also serve to stabilize the CLP domain as well. The loading of drug molecules of the other drug/ECnV combinations was shown to have a limited effect (<1 °C change in $T_m$) on the stability of the CLP domain.

Furthermore, as described above, the assembled ECnVs can be disassembled, as monitored via DLS, when the CLP triple helices unfold (data not shown). Therefore, all three ECnVs with encapsulated drug molecules (Dex-CF, Dox, MTX) are competent for disassembly with a thermal trigger (temperature above $T_m$), which suggests opportunities in hyperthermal drug delivery. Compared to previously published studies of these CLPs,[61] our data show similar $T_m$ (57.2 °C) values for the $G_8$-containing sequences ($Y_6$-$G_8$, $F_6$-$G_8$), while $W_6$-$G_8$ exhibits an elevated $T_m$, which could possibly relate to an increased extent of hydrophobic interactions of the $W_6$. Similar observations have also been previously reported; Qin et al. showed that the inclusion of W in the ELP domain can significantly stabilize the unfolding of the CLP after the ELP coacervates above its $T_t$.[47] Other work conducted by Egli et al. has also indicated that the $T_m$ of a CLP system increases significantly once conjugated with a hydrophobic moiety.[18] Additional optimization is clearly required to decrease the $T_m$ to a reasonable temperature to apply in hyperthermal therapy, which could be achieved by decreasing the length of the CLP as has been reported for dendrimer−collagen systems.[62]

**Vesicle Characterization.** To evaluate to what extent the loading of cargo molecules (Dex-CF, Dox, MTX) may


https://doi.org/10.1021/acs.biomac.3c01361
Biomacromolecules 2024, 25, 2408−2422

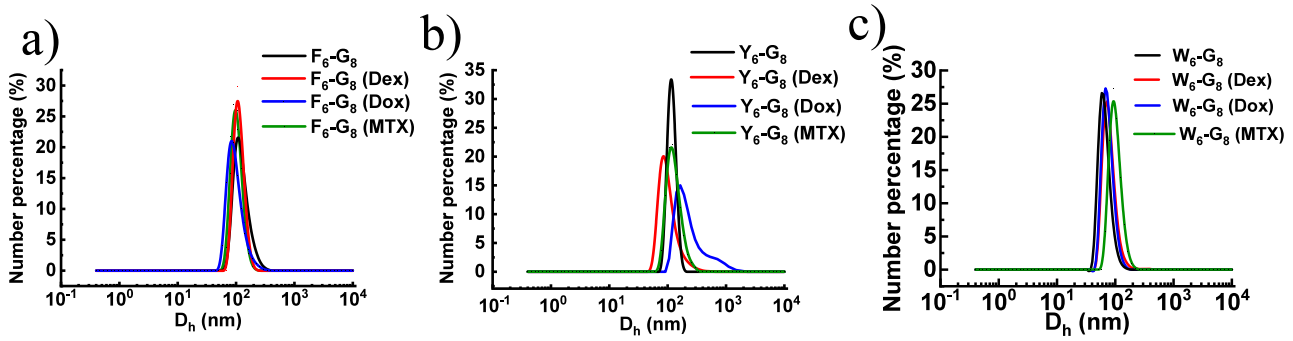


**Figure 3.** Hydrodynamic diameter distribution data obtained from dynamic light scattering (DLS) measurements of the ECnVs, with and without drug molecules encapsulation, at 37 °C. (a) $F_6$-$G_8$; (b) $Y_6$-$G_8$; (c) $W_6$-$G_8$.

influence the hydrodynamic diameter of the ECnVs, dynamic light scattering (DLS) was conducted for each ECnV/cargo combination in aqueous solution at 37 °C (Figure 3). As shown in the figure, each of the ECnVs and drug/ECnV combinations exhibited hydrodynamic diameters in the range of 50−100 nm dependent on the identity of the ECnV and the drug cargo. The diameter of $F_6$-$G_8$ ($D_h$ = 113.6 ± 6.7 nm) changed slightly after the loading of Dex-CF ($D_h$ = 110.5 ± 9.7 nm), MTX ($D_h$ = 102.8 ± 8.9 nm), and Dox ($D_h$ = 91.1 ± 5.5 nm), indicating that the loading of these three drug molecules did not have a significant impact on the hydrodynamic diameter of $F_6$-$G_8$ (Figure 3a). The diameter of $Y_6$-$G_8$ ($D_h$ = 118.0 ± 14.1 nm) decreased slightly after the loading of Dex-CF ($D_h$ = 89.6 ± 5.2 nm) and not significantly after loading of MTX ($D_h$ = 118.8 ± 7.8 nm)(Figure 3b) but exhibited a significant increase after the loading of the Dox ($D_h$ = 283.5 ± 88.6 nm) along with a significant increase in polydispersity, suggesting either the presence of large-size spherical particles or potentially nonspherical particles. Further TEM investigation was conducted to determine the morphological features of these Dox-loaded $Y_6$-$G_8$ ECnVs (Figure 4, see data and discussion below). The $W_6$-$G_8$ ($D_h$ = 65.8 ± 5.4 nm) exhibited a similar diameter after the loading of Dex-CF ($D_h$ = 74.9 ± 5.6 nm) and Dox ($D_h$ = 74.1 ± 5.9 nm), which suggests

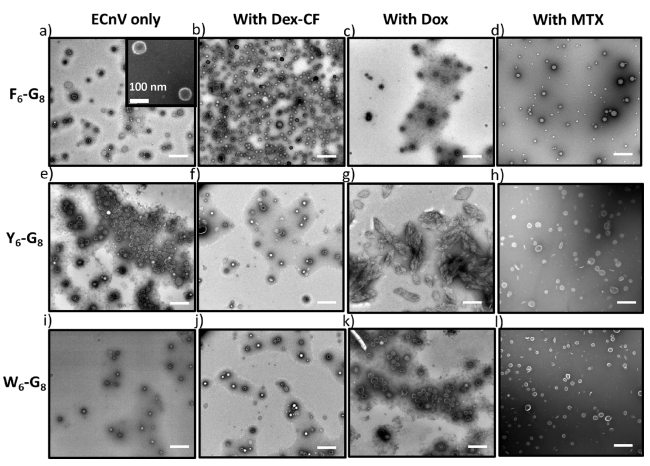


**Figure 4.** TEM images of various ECnVs with different cargo molecules encapsulated. (a) $F_6$-$G_8$, the inset is a TEM image at a higher magnification of $F_6$-$G_8$ showing the vesicle configuration. (b) $F_6$-$G_8$/Dex-CF; (c) $F_6$-$G_8$/Dox; (d) $F_6$-$G_8$/MTX; (e) $Y_6$-$G_8$; (f) $Y_6$-$G_8$/Dex-CF; (g) $Y_6$-$G_8$/Dox; (h) $Y_6$-$G_8$/MTX; (i) $W_6$-$G_8$; (j) $W_6$-$G_8$/Dex-CF; (k) $W_6$-$G_8$/Dox; (l) $W_6$-$G_8$/MTX. Stained with 1% PTA at 37 °C. Scale bars: 500 nm.

that the loading of the Dex-CF and Dox do not have a significant impact on the hydrodynamic diameter of $W_6$-$G_8$ (Figure 3c). However, the loading of MTX ($D_h$ = 99.3 ± 8.0 nm) in $W_6$-$G_8$ resulted in a significant increase in $D_h$, which was similar to behavior reported for an mPEG−PCL polymersome system after MTX loading, owing to the previous report to the swelling of the hydrophilic domain of mPEG.[63]

To further investigate the morphological changes of the ECnVs after drug loading, TEM imaging was conducted at 37 °C. Samples were prepared as described in the sample preparation section. As expected, $F_6$-$G_8$ showed low dispersity after the loading of three drug molecules (Figures 4a−d and S15 for cryogenic TEM image) as did $W_6$-$G_8$ (Figure 4i−l). As indicated in the DLS data in Figure 3b, the loading of Dex-CF and MTX in $Y_6$-$G_8$ yielded vesicles of low dispersity (Figure 4e,f,h), although the loading of Dox in the $Y_6$-$G_8$ resulted in high polydispersity and a significant increase in the apparent hydrodynamic diameter; the TEM data for the Dox/$Y_6$-$G_8$ samples indicates that the Dox-loaded $Y_6$-$G_8$ formed plate-like structures (278 ± 80 × 286 ± 89 nm). Similar observations of plate-like structures for other ELP-CLP sequences have been reported previously by our group[47,61] in which several factors affected the resulting assembled morphology, such as the relative lengths of the ELP and CLP domains and the hydrophobicity of the ELP domain. In this work, since the relative length of the ELP/CLP is unchanged, the morphology transition to a nanostructure with lower surface curvature is likely due to an increase in cargo/ELP interactions in the ELP domain. Therefore, at 3 days of Dox release, the Dox/$Y_6$-$G_8$ samples were characterized via TEM; the data indicate a morphological transition from platelets to vesicles (Figure S16). The correlation of the morphology changes with a threshold Dox concentration, and the fact that intact vesicles are recovered from the plate-like structures with Dox release, which corroborates that the interaction of the drug with the peptide domains is likely the origin of these observations. Therefore, the potential interactions of Dox and Dex-CF with the ELP domains in assembled ECnVs were evaluated via fluorescence resonance energy transfer experiments. The fluorescence resonance energy transfer (FRET) assay has been widely utilized to determine the distance between molecules and to assess intramolecular interactions,[64] because FRET can only occur when the donor and acceptor molecules are in close proximity (~3 nm).[65] To conduct these experiments, the ELP domains of the ECnVs ($F_6$-$G_8$, $Y_6$-$G_8$, $W_6$-$G_8$) were covalently conjugated with AZ 350 (for characterization of Dex-CF-loaded ECnVs) and AZ 405 (for Dox-loaded ECnVs). Corresponding drug molecules were


https://doi.org/10.1021/acs.biomac.3c01361
Biomacromolecules 2024, 25, 2408−2422

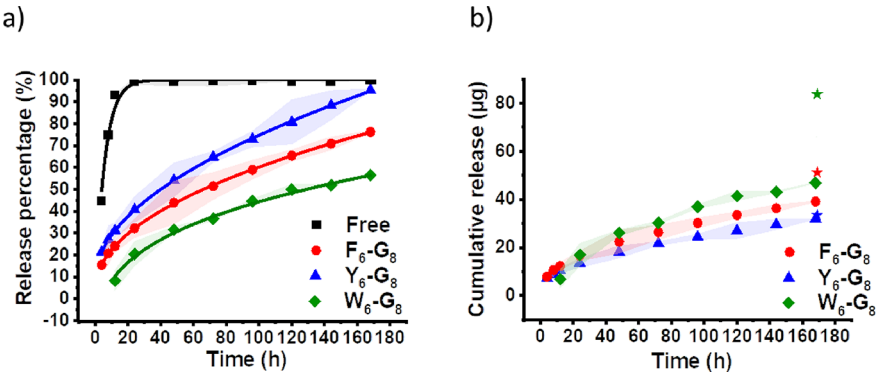


**Figure 5.** Dex-CF encapsulation efficiency and release kinetics profile. (a) Cumulative percentage release of Dex-CF up to 7 days; (b) cumulative amount of release of Dex-CF up to 7 days. The star in the figure indicates the total amount of encapsulated Dex-CF, and the error bars are rendered as the colored area around the curve. ($n$ = 3).

**Table 2. Summary of Dex-CF Encapsulation, EE, LC, and the Constants of the Korsmeyer–Peppas Release Model ($n$ = 3)**

| ECnVs | encapsulated Dex-CF ($\mu$g) | Dex-CF EE (%) | Dex-CF LC (%) | $K_{kp}$ | $n$ | $R^2$ |
|---|---|---|---|---|---|---|
| $F_6$-$G_8$ | 51.4 ± 6.5 | 20.5 ± 2.6 | 20.5 ± 2.6 | 6.3 | 0.48 Quasi-Fickian | 0.999 |
| $Y_6$-$G_8$ | 33.4 ± 3.5 | 13.4 ± 1.4 | 13.4 ± 1.4 | 6.1 | 0.52 Non-Fickian | 0.999 |
| $W_6$-$G_8$ | 83.8 ± 1.8 | 33.5 ± 0.7 | 33.5 ± 0.7 | 18.9 | 0.29 Quasi-Fickian | 0.999 |

encapsulated in the ECnVs as described above, and centrifugation was conducted to remove the unencapsulated drug and unreacted fluoroprobes. MTX-loaded ECnVs were not examined due to the nonfluorescent nature and high hydrophilicity of MTX. The AZ 350-labeled ECnVs were excited at 350 nm, which is outside of the excitation range of the Dex-CF. The Dex-CF emission peak detected at 520 nm (Figure S17a) indicates that Dex-CF has been excited, likely due to the emission of the AZ350 within the excitation range of Dex-CF, suggesting close contact (~3 nm) of the ELP domain and the Dex-CF. Because the ELP domain is separated from any Dex-CF in solution by the 7.5 nm thickness of the CLP triple helical domain,[61] any FRET that occurs must likely arise from interactions within the ELP domain and not between any free Dex-CF in the solution with the ECnV peptide bilayer. Similarly, emission peaks at 590 nm for the Dox encapsulation were also observed when the system was excited at 405 nm (Figure S17b), which is outside the excitation range of Dox, suggesting the occurrence of FRET and thus a close proximity of Dox and the AZ405. These results are consistent with the enrichment of both Dex-CF and Dox in the ELP domain of these ECnVs.

**Cargo Release Kinetics from ECnVs.** To determine the release kinetics of Dex-CF, Dox, and MTX from ECnVs, drug encapsulation and in vitro release studies were conducted using a dialysis method under physiologically relevant conditions as described in the methods and materials section. The encapsulation efficiency (EE) and loading capacity (LC) for each cargo/ECnV combination were determined using eqs 1 and 2, as described in the experimental section.

*Dex-CF Release Kinetics.* After collecting the release solution at the indicated time points, the cumulative percentage release of Dex-CF per sample was calculated using eq 3 (experimental section). Because of the hydrophobicity of the Dex-CF (with an octanol–water partition coefficient of >1.89), unencapsulated and undissolved Dex-CF will likely remain in the centrifuged ECnV pellets, complicating the measured release curve, which would then represent contributions from both unencapsulated and encapsulated Dex-CF. In order to account for diffusion across the dialysis membrane of any unencapsulated Dex-CF in the samples, a control experiment to monitor the rate of release of free Dex-CF across the dialysis membrane was conducted, under Dex-CF concentrations based on the measured EE of the Dex-CF in the various ECnVs. The EE (all $n$ = 3) for $F_6$-$G_8$ was 20.5 ± 2.6%, for $Y_6$-$G_8$ 13.4 ± 1.4%, and for $W_6$-$G_8$ 33.5 ± 0.7%; therefore, free Dex-CF samples with 79.5, 86.6, and 66.5% of the initial Dex-CF were employed in the free Dox diffusion control experiments. These release profiles of free drug were then subtracted from the release profile of the unwashed drug-loaded ECnVs; the "baseline" corrected data are shown in Figure 5. The data in Figure 5 show that the release rate of Dex-CF from the ECnVs is slower than the free diffusion of Dex-CF across the dialysis membrane, as anticipated; the release data from ECnVs was fit to the Korsmeyer–Peppas model ($R^2$=0.999), while the free Dex-CF release cleanly fits to a first-order release model as expected. The numeric coefficient ($n$) from the Korsmeyer–Peppas model is used to describe the mechanism of the release;[66] the values for Dex-CF release from $F_6$-$G_8$ ($n$ = 0.48) and $W_6$-$G_8$ ($n$ = 0.29) were less than 0.50, which indicates a Fickian diffusion mechanism, while the value for $Y_6$-$G_8$ ($n$ = 0.52) was slightly larger than 0.50, which indicates a mixed mechanism of both Fickian diffusion and dissolution.[49] The $k$ in the first-order release model is the rate constant for concentration-dependent release. All the EE, LC, $n$, and $R^2$ data of the Dex-CF release studies are shown in Table 2.

*Dox Release Kinetics.* The Dox encapsulation and release studies were conducted in a separate experiment with the same set of ECnVs. After collecting the release solution at the indicated time points, the cumulative percentage release of Dox per sample was calculated using eq 3 where the $M_{drugloaded}$


https://doi.org/10.1021/acs.biomac.3c01361
Biomacromolecules 2024, 25, 2408–2422

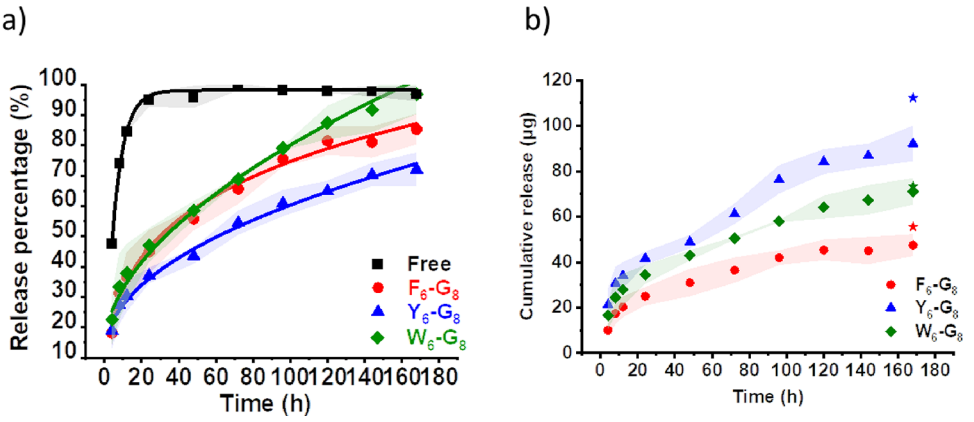


**Figure 6.** Dox encapsulation efficiency and release kinetics profile. (a) Cumulative percentage release of Dox up to 7 days; (b) cumulative amount release of Dox up to 7 days. The star in the figure indicates the total amount of encapsulated Dox, and the error bars are rendered as the colored area around the curve ($n$ = 3).

**Table 3. Summary of Dox encapsulation, EE, LC, and the Constants of the Korsmeyer–Peppas Release Model ($n$ = 3)**

| ECnVs | encapsulated Dox ($\mu$g) | Dox EE (%) | Dox LC (%) | $K_{kp}$ | $n$ | $R^2$ |
|---|---|---|---|---|---|---|
| $F_6$-$G_8$ | 55.6 ± 6.3 | 22.2 ± 2.1 | 22.2 ± 2.1 | 47.7 | 0.20 Quasi-Fickian | 0.999 |
| $Y_6$-$G_8$ | 112.4 ± 4.2 | 44.9 ± 1.2 | 44.9 ± 1.2 | 5.8 | 0.47 Quasi-Fickian | 0.999 |
| $W_6$-$G_8$ | 73.4 ± 3.6 | 29.4 ± 1.1 | 29.4 ± 1.1 | 5.6 | 0.54 Non-Fickian | 0.999 |

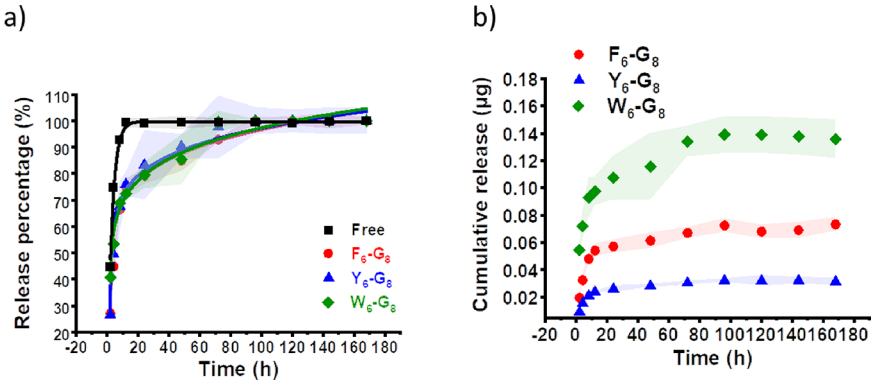


**Figure 7.** MTX encapsulation efficiency and release kinetics profile. (a) Cumulative percentage release of MTX up to 7 days; (b) cumulative release of MTX up to 7 days, and the error bars are rendered as the colored area around the curve ($n$ = 3).

is the mass of the encapsulated Dox. Since the Dox is less hydrophobic than the Dex-CF (with an octanol–water partition coefficient of 0.52 (<1.89 for Dex-CF)) and the release curve did not show a burst release (Figure 6), subtraction of the diffusion curve of free drug was not conducted for these drug/ECnV combinations. It is clearly shown that the release of Dox from ECnVs is slower than the free Dox diffusion (black curve in Figure 6a) across the dialysis membrane. The Dox release from the ECnVs was fit to a Korsmeyer–Peppas model ($R^2$=0.999), while the free Dox release was fit to a first-order release model. As for Dex-CF, the numeric coefficients ($n$) from the Korsmeyer–Peppas model were less than 0.50 for $F_6$-$G_8$ ($n$ = 0.20) and $Y_6$-$G_8$ ($n$ = 0.47), suggesting a Fickian diffusion mechanism. The slightly higher value for $W_6$-$G_8$ ($n$ = 0.54) may suggest a mixed mechanism of both Fickian diffusion and dissolution as we reported before for other molecules with greater water solubility (vancomycin).[49] The $k$ in the first-order release model is the rate constant for concentration-dependent release. All of the EE, LC, $n$, and $R^2$ data of the Dox release studies are shown in Table 3.

*MTX Release Kinetics.* The MTX encapsulation and release kinetics were evaluated in separate experiments with three synthetic repeats for each ECnV. As above, after collecting the release solution at the indicated time points, the cumulative percentage release of MTX per sample was calculated using eq 3 where the $M_{drugloaded}$ will be the mass of the encapsulated MTX. The MTX is more hydrophilic than Dox and a greater extent of burst release was observed for MTX from all three ECnVs, which may suggest lower interactions of MTX with any of the ELPs.

Similar burst release of MTX from other drug carriers including liposomes[67] and microparticles[68] has also been previously reported. It is clear from the data that the rate of release of MTX from the ECnVs is slower than the free MTX diffusion (black curve in Figure 7) across the dialysis


https://doi.org/10.1021/acs.biomac.3c01361
Biomacromolecules 2024, 25, 2408–2422

Table 4. Summary of MTX encapsulation, EE, LC, and the Constant of the Korsmeyer−Peppas Release Model ($n$ = 3)

| ECnVs | encapsulated MTX ($\mu$g) | MTX EE (%) | MTX LC (%) | $K_{kp}$ | $n$ | $R^2$ |
|---|---|---|---|---|---|---|
| $F_6$-$G_8$ | 73.4 ± 5.0 | 28.7 ± 1.6 | 28.7 ± 1.6 | 52.9 | 0.13 Quasi-Fickian | 0.993 |
| $Y_6$-$G_8$ | 32.1 ± 2.4 | 12.6 ± 1.1 | 12.6 ± 1.1 | 55.5 | 0.12 Quasi-Fickian | 0.973 |
| $W_6$-$G_8$ | 135.9 ± 14.2 | 53.9 ± 5.2 | 53.9 ± 5.2 | 52.2 | 0.14 Quasi-Fickian | 0.974 |

membrane. Therefore, again as above, the MTX release from ECnVs was fit to a Korsmeyer−Peppas model ($R_{F_6G_8}{}^2$= 0.993, $R_{Y_6-G_8}{}^2$= 0.973, $R_{W_6-G_8}{}^2$= 0.974), while the free MTX release was fit to a first-order release model. The numeric coefficients ($n$) from the Korsmeyer−Peppas model for $F_6$-$G_8$ ($n$ = 0.13), $Y_6$-$G_8$ ($n$ = 0.12), and $W_6$-$G_8$ ($n$ = 0.14) were all less than 0.50 in this set of experiments, suggesting a Fickian diffusion mechanism for MTX as for Dex-CF and Dox. The $k$ in the first-order release model, as above, is the rate constant for concentration-dependent release. All the EE, LC, $n$, and $R^2$ data of the MTX release studies are shown in Table 4.

The encapsulation of drugs within nanocarriers serves to protect cargo from degradation and enhances sustained release, which can result in improved pharmacokinetics and reduced off-target effects. The ECnVs supported sustained release of all three cargo molecules (Dex-CF, Dox, MTX) compared to the free drug diffusion, suggesting a barrier to diffusion that could arise from physicochemical interactions between the cargo and the ELP (or CLP) domains of the ECnVs. For the Dex-CF, the encapsulation data indicates that the $W_6$-$G_8$ has the highest EE (33.5 ± 0.7%), followed by the $F_6$-$G_8$ (20.5 ± 2.6%), with the $Y_6$-$G_8$ exhibiting the lowest EE (13.4 ± 1.4%). In addition to these differences in the EE, the release curves for these three sequences also showed significant differences from each other ($W_6$-$G_8$ vs $F_6$-$G_8$ and $Y_6$-$G_8$ vs $F_6$-$G_8$: $0.001 < p < 0.01$, $Y_6$-$G_8$ vs $W_6$-$G_8$: $p < 0.001$), which suggests that there may be different degrees of physical interaction between drugs and the ELP domains. Phenylalanine, tyrosine, and tryptophan all exhibit inter- and intramolecular $\pi-\pi$ interactions, consistent with their ability to support sustained release of Dex-CF from these three ECnV sequences.[48,52] Our observations are also in agreement with previous studies that have shown that Dex-CF has stronger hydrophobic interactions with tryptophan than with tyrosine or phenylalanine,[69] consistent with the longer retention and higher EE of Dex-CF within the $W_6$-$G_8$.

As for the Dox, $Y_6$-$G_8$ has the highest EE (44.9 ± 1.2%), followed by $W_6$-$G_8$ (29.4 ± 1.1%), with $F_6$-$G_8$ (22.2 ± 2.1%). The EE and the release curve for $Y_6$-$G_8$ showed the highest statistically significant difference relative to the release from $W_6$-$G_8$ and $F_6$-$G_8$ ($p < 0.001$), while the data for $W_6$-$G_8$ and $F_6$-$G_8$ showed minimal significant differences between each other ($0.01 < p < 0.05$). These data suggest a higher degree of physical interaction between Dox and the $Y_6$-$G_8$, which is also consistent with our TEM observations that the morphology switches from vesicles to platelets for $Y_6$-$G_8$ after the encapsulation of Dox, reverting to vesicles after 3 days of Dox release (~50% released, ~ 61 $\mu$g of Dox remained encapsulated in the $Y_6$-$G_8$ ECnV); these observations suggest the minimal amount of Dox necessary to trigger the morphological change. According to the release profile, the maximum amount of Dox encapsulated in $F_6$-$G_8$ was ~55 $\mu$g, which is consistent with the lack of a morphological transition for this ECnV. Although the $W_6$-$G_8$ ECnVs encapsulated greater than 61 $\mu$g (~73 $\mu$g) of Dox, they exhibit a 45% smaller hydrodynamic diameter (65 vs 118 nm) compared to $Y_6$-$G_8$, which will result in a larger number of ECnVs (~3.3 times). The amount of encapsulated Dox within each ECnV may therefore be below the minimum required for a morphological transition. Furthermore, other work has also indicated strong $\pi-\pi$ interactions between Y and Dox, where a pronounced redshift was observed from Dox-loaded nanoparticles comprising poly tyrosine.[70] These interactions are likely the origin of the high EE and LC (and morphological shift) for the $Y_6$-$G_8$/Dox pair reported here.

Our observations of morphological changes with different extents of drug loading are also consistent with previous reports. The Wang group showed that the weight ratio of Docetaxel/amphiphilic PAMAM-*b*-OEG co-dendrimer could affect the shapes of nanostructures; with greater amounts of drug encapsulation, a morphological change from nanospheres to nanosheets was observed, although there was not a large difference in drug release kinetics for the different nanostructures.[71] Lim et al. also reported nanocarrier morphological differences with identical release kinetics of olaparib, which serves as a medication for the maintenance treatment of BRCA-mutated advanced ovarian cancer in adults, from spherical micelles compared with worm-like micelles assembled with poly(2-oxazoline).[72] Guo et al. investigated the biological applications of hydroxy camptothecin nanoparticles based on poly/oligo (ethylene glycol) with nanosphere and nanorod morphologies in which similar drug release rates were observed, although the nanospheres exhibited a slightly greater rate of drug release than the nanorods.[73] Previous studies have highlighted strong $\pi-\pi$ interactions in a Y-enriched system; the higher Dox encapsulation efficiency observed with $Y_6$-$G_8$ might suggest enhanced $\pi-\pi$ interactions.

In contrast to our results for the Dex-CF and Dox encapsulation and release, the release curves of MTX from all of the ECnV carriers indicate a similar release rate, with a burst release on day 1. Because of the hydrophilicity of the MTX, it is possible that the cargo molecules do not interact strongly with the ELP domain and thus might be located both within the ELP-CLP peptide bilayer and the aqueous core of the ECnVs.[49] Other work on the encapsulation of MTX in PEG-lipid bilayer vesicles is consistent with this supposition; the hydrophilic MTX was indicated to be located inside the aqueous core and showed a burst release of greater than 70% within 24 h.[74] Although the observed burst release in the present work may result from the low interaction between the ELP and the MTX, the release profiles clearly show slower release than the free drug diffusion across the dialysis membrane, consistent with some MTX/ECnV interaction. Furthermore, the $T_m$ increase after the MTX encapsulation also indicates a possible interaction between CLP domain and the MTX. These observations would be consistent with


https://doi.org/10.1021/acs.biomac.3c01361
Biomacromolecules 2024, 25, 2408−2422

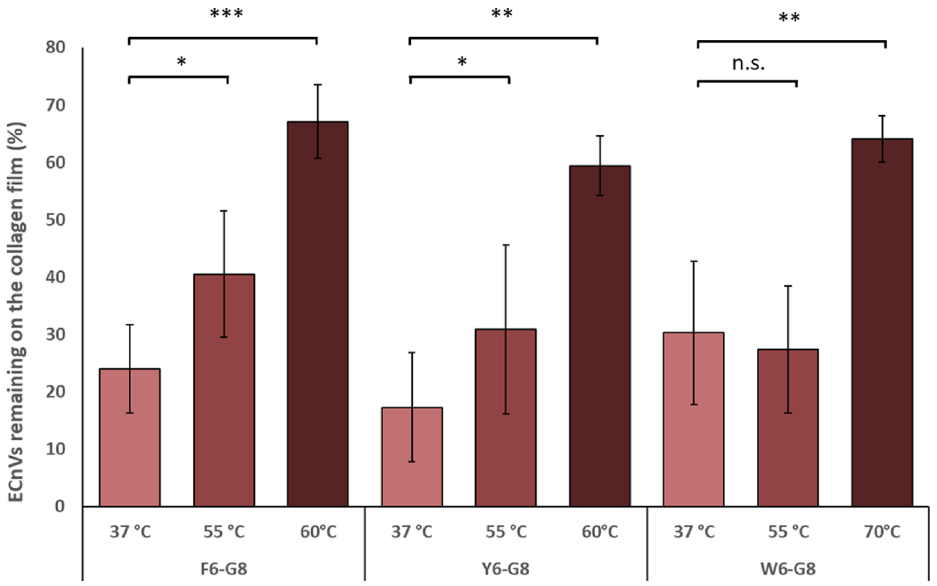


**Figure 8.** 2D Collagen-binding assay for $W_6$-$G_8$, $Y_6$-$G_8$, and $F_6$-$G_8$ at different temperatures. (n.s.: $p > 0.05$; "*": $0.01 < p < 0.05$; "**": $0.001 < p < 0.1$; "***": $p < 0.001$) ($n = 4$).

possible interactions of MTX with the CLP domain, as suggested in previous studies. Narayani et al. reported the encapsulation and release of MTX from a collagen-p(HEMA) hydrogel, suggesting that interactions between collagen and MTX supported sustained release.[75] Although in our studies there was no statistically significant difference in the observed release rates of MTX from the three ECnVs, the EE and LC showed significant differences, where $W_6$-$G_8$ showed the highest EE (53.9 ± 5.2%), followed by $F_6$-$G_8$ (28.7 ± 1.6%) and $Y_6$-$G_8$ (12.6 ± 1.1%). We note that the differences in the EE values observed may be attributable to the smaller diameter of the $W_6$-$G_8$ vesicles (mentioned above), which would result in a greater number (per ELP-CLP mass) of $W_6$-$G_8$ vesicles and also in a higher surface area of CLP to bind MTX, which could result in a higher EE and LC for encapsulation in the core of the vesicles and/or via interactions with the CLP.

**2D Collagen-Binding Assay.** As discussed above, current clinical regimens employ intra-articular injection of dexamethasone for the treatment of OA. Because of its poor bioavailability due to the high turnover of the synovial fluid, the injections are conducted repeatedly and at a high dosage of Dex-CF,[29−31] resulting in higher off-target effects.[76] According to our previous study, ECnVs have the ability to be retained in the murine knee joint for up to 240 h, suggesting the potential for targeted retention and longer-term Dex release.[50] Moreover, in other ECM-related pathologies involving abnormal remodeling of tissues (e.g., cancer and rheumatoid arthritis (RA)) collagen-targeting also has similar potential. Both Dox (the widely used antitumor drug) and MTX (an anti-inflammatory drug for RA) share a significant clinical drawback of severe off-target effects, so ECnV platforms may be particularly useful for their encapsulation and delivery.

Preliminary cell compatibility studies were therefore conducted with the ECnVs. Studies of NH3T3 cell metabolic activity after 4 days of exposure to ECnVs and Dex-CF-loaded ECnVs (Figure S18) shows that the ECnVs alone did not exhibit a decrease in proliferation, suggesting a high cell viability. Furthermore, the Dex-CF-loaded ECnVs show a relatively smaller decrease in proliferation compared to Dex-CF alone, suggesting that encapsulation using ECnV improves the cell viability. Studies of ECnV immunogenicity are underway as a part of separate studies outside of the scope of this initial report; no significant immunogenicity is expected as both ELP[77] and CLP[78] have been recognized as excellent candidates for nonimmunogenic materials.

Targeted binding of ECnVs to collagen followed by sustained cargo release may improve the efficacy of lower Dox or MTX doses than can be currently employed, thus offering opportunities to lower overall dosage and minimize off-target effects. Accordingly, a 2D collagen-binding assay was conducted on collagen I (rat tail)-coated wells of a 96-well plate. Labeled ECnVs (labeling confirmed by the elimination of the negative zeta-potential (Figure S19) and morphology of labeled ECnVs confirmed via negatively stained TEM (Figure S20)) were preheated at two different temperatures (55 °C and at ∼ $T_m$) and then applied to the collagen films overnight at 37 °C followed by three washes the next day, as described in the experimental section. The $T_m$ incubation temperatures were identified for specific ECnVs and were based on the CLP unfolding temperature of each sequence, where 60 °C was chosen for $F_6$-$G_8$ ($T_m$ = 57.3 °C) and $Y_6$-$G_8$ ($T_m$ = 58.4 °C), and 70 °C was chosen for $W_6$-$G_8$ ($T_m$ = 69.4 °C), as it has been previously shown that the hybridization between CLP and the type I collagen occurs primarily through hybridization of single-stranded CLP with the collagen matrix.

The 2D collagen-binding studies (Figure 8) showed that all ECnVs generally showed an increased amount of binding/retention on the collagen films with increases in preincubation temperatures. For $F_6$-$G_8$ and $Y_6$-$G_8$, there were significant differences in binding of the ECnVs to collagen with preincubation at 37 and 55 °C and also between 37 and 60 °C, as expected based on the CD data indicating their $T_m$ between 55 and 60 °C. There was no significant difference in binding percentage between 37 and 55 °C for $W_6$-$G_8$, but there was a significant difference between 37 and 70 °C. The CD data supported these findings, showing similar triple helix molar ellipticity at 55 °C for $W_6$-$G_8$ compared to 37 °C and reduced molar ellipticity at 70 °C (Figure S13).

This 2D collagen-binding assay confirmed the capability of ECnVs of different compositions to bind to collagen type I


https://doi.org/10.1021/acs.biomac.3c01361
Biomacromolecules 2024, 25, 2408−2422

films, and that this binding relates as expected to the availability of single-stranded CLP in an ECnV sample. The binding percentage observed with preincubation near the $T_m$ temperature (either 60 or 70 °C depending on the CLP sequence) was significantly greater than that at 37 or 55 °C for all three sequences ($F_6$-$G_8$, $Y_6$-$G_8$, and $W_6$-$G_8$). Recent work reported by Arlotta et al. showed the possibility of using CLP with the sequence $(GPO)_9$ as a targeting molecule to localized the anti-TNF$\alpha$ therapeutic infliximab (iFab) to arthritic tissues.[79] Another study conducted by Zitnay et al. showed the feasibility of utilizing CLP binding to damaged collagen for detecting molecular level, subfailure damage in rat-tail tendon.[80] The high $T_m$ of these previously reported CLP sequences (75 °C), however, may limit use of these particular CLPs in some applications. In the current work, we have demonstrated the possibility of lower preincubation temperatures for localizing cargo-laden ECnVs to collagen-containing substrates. These results suggest significant opportunities in the design of CLP-stabilized nanoparticles, which would be capable of binding to collagen and releasing cargo at elevated temperatures, as well as in the design of CLP-based materials for tissue engineering, regenerative medicine, and bioimaging applications.

## CONCLUSIONS

In summary, our data show that ECnVs can successfully encapsulate and deliver hydrophobic small-molecule drugs while maintaining thermal stability of the ECnV, with sustained release of cargo for up to 7 days. The release rate of hydrophobic drugs was slower than that of hydrophilic drugs in the ECnVs studied, presumably due to strong hydrophobic interactions between cargo and the ELP domains. However, encapsulation of hydrophilic drugs was also possible, with high drug loading that may be enabled by encapsulation in the ECnV lumen and by interactions with CLP. Our studies also suggest the colocalization of the hydrophobic cargo within the ELP domain, providing further evidence for the key role of the ELP domains to tune cargo loading in and release from ECnVs. The 2D collagen-binding assays demonstrate the collagen targeting ability of each of these ECnVs, which may have implications for the future use of the general ECnV platform for drug delivery and disease treatment. Additionally, the potential for customizing the release rate through subtle alterations in the sequence of the ELPs adds a layer of versatility, enabling tailored delivery profiles to meet diverse therapeutic needs, making them adaptable and potentially more effective in targeted therapy.

## ASSOCIATED CONTENT

### Supporting Information

The Supporting Information is available free of charge at https://pubs.acs.org/doi/10.1021/acs.biomac.3c01361.

Peptide synthesis, cryogenic-transmission electron microscopy (Cryo-TEM), cell metabolic activity and viability, and supplementary figures (PDF)

## AUTHOR INFORMATION


### Corresponding Author

**Kristi L. Kiick** − *Department of Materials Science and Engineering and Department of Biomedical Engineering, University of Delaware, Newark, Delaware 19716, United States;* orcid.org/0000-0001-8587-0301; Phone: 302-831-6592; Email: kiick@udel.edu

### Authors

**Haofu Huang** − *Department of Materials Science and Engineering, University of Delaware, Newark, Delaware 19716, United States;* orcid.org/0000-0003-1837-8530

**Jeongmin Hwang** − *Department of Biomedical Engineering, University of Delaware, Newark, Delaware 19716, United States;* orcid.org/0000-0001-8799-3209

**Sudha Anilkumar** − *Department of Biomedical Engineering, University of Delaware, Newark, Delaware 19716, United States*

Complete contact information is available at: https://pubs.acs.org/10.1021/acs.biomac.3c01361


### Author Contributions

H.H. and K.L.K. contributed to the study of concepts and design. Material preparation, data collection, and analysis were performed by H.H, J.H., and S.A. The first draft of the manuscript was written and edited by H.H. and K.L.K. All authors read and approved the final manuscript.

### Notes

The authors declare no competing financial interest.

## ACKNOWLEDGMENTS

This work was supported by grants from the National Institutes of Health (R01AR067247, R01DK130662, and P30GM110758) and the National Science Foundation (CBET1605130 and CBET2023668). The authors acknowledge the use of facilities and instrumentation supported by NSF through the University of Delaware Materials Research Science and Engineering Center, DMR-2011824. The microscopy equipment employed in the studies was acquired with shared instrumentation grants (S10 RR027273 and S10 OD016361) and access was supported by the NIH-NIGMS (P20 GM103446), the NIGMS (P20 GM139760), and the State of Delaware. The views expressed here are the responsibility of the authors and do not necessarily reflect the position of the funding agencies. The authors also thank Dr. Luisa Palmese for her invaluable assistance in generating the cell metabolism data in the Supporting Information and thank Yao Tang for his assistance in generating the cryogenic TEM data in the Supporting Information.

## REFERENCES

(1) Sushant, T., Avinash, G. O. S. *Nanomedicine Market by Modality (Diagnostics and Treatment), Application (Drug Delivery, Diagnostic Imaging, Vaccines, Regenerative Medicine, Implants, and Others), and Indication (Clinical Oncology, Infectious Diseases, Clinical Cardiology, Orthopedics*, Allied Market Research 2022.

(2) Vert, M.; Doi, Y.; Hellwich, K. H.; Hess, M.; Hodge, P.; Kubisa, P.; Rinaudo, M.; Schué, F. Terminology for Biorelated Polymers and Applications (IUPAC Recommendations 2012). *Pure Appl. Chem.* **2012**, *84* (2), 377−410.

(3) Baroli, B.; Ennas, M. G.; Loffredo, F.; Isola, M.; Pinna, R.; López-Quintela, M. A. Penetration of Metallic Nanoparticles in Human Full-Thickness Skin. *J. Invest. Dermatol.* **2007**, *127* (7), 1701−1712.

(4) Brown, T. D.; Habibi, N.; Wu, D.; Lahann, J.; Mitragotri, S. Effect of Nanoparticle Composition, Size, Shape, and Stiffness on Penetration across the Blood-Brain Barrier. *ACS Biomater. Sci. Eng.* **2020**, *6* (9), 4916−4928.

(5) Thi, T. T. H.; Suys, E. J. A.; Lee, J. S.; Nguyen, D. H.; Park, K. D.; Truong, N. P. Lipid-Based Nanoparticles in the Clinic and Clinical Trials: From Cancer Nanomedicine to COVID-19 Vaccines. *Vaccines* **2021**, *9* (4), 359.
(6) Li, W.; Szoka, F. C. Lipid-Based Nanoparticles for Nucleic Acid Delivery. *Pharm. Res.* **2007**, *24* (3), 438−449.
(7) Fang, E.; Liu, X.; Li, M.; Zhang, Z.; Song, L.; Zhu, B.; Wu, X.; Liu, J.; Zhao, D.; Li, Y. Advances in COVID-19 MRNA Vaccine Development. *Signal Transduct. Target. Ther.* **2022**, *7* (1), 94.
(8) Akbarzadeh, A.; Rezaei-Sadabady, R.; Davaran, S.; Joo, S. W.; Zarghami, N.; Hanifehpour, Y.; Samiei, M.; Kouhi, M.; Nejati-Koshki, K. Liposome: Classification, Preparation, and Applications. *Nanoscale Res. Lett.* **2013**, *8* (1), 102.
(9) Che, H.; van Hest, J. C. M. Adaptive Polymersome Nanoreactors. *ChemNanoMat* **2019**, *5* (9), 1092−1109.
(10) Liu, X.; Wu, Z.; Cavalli, R.; Cravotto, G. Sonochemical Preparation of Inorganic Nanoparticles and Nanocomposites for Drug Release-A Review. *Ind. Eng. Chem. Res.* **2021**, *60* (28), 10011−10032.
(11) Barenholz, Y. C. Doxil® — The First FDA-Approved Nano-Drug: Lessons Learned. *J. Controlled Release* **2012**, *160* (2), 117−134.
(12) Guimarães, D.; Cavaco-Paulo, A.; Nogueira, E. Design of Liposomes as Drug Delivery System for Therapeutic Applications. *Int. J. Pharm.* **2021**, *601*, No. 120571.
(13) Lee, J. S.; Feijen, J. Polymersomes for Drug Delivery: Design, Formation and Characterization. *J. Controlled Release* **2012**, *161* (2), 473−483.
(14) Huang, H.; Kiick, K. Peptide-Based Assembled Nanostructures That Can Direct Cellular Responses. *Biomed. Mater.* **2022**, *17* (6), No. 062002.
(15) Caiaffa, K. S.; dos Santos, V. R.; Abuna, G. F.; Santos-Filho, N. A.; Cilli, E. M.; Sakai, V. T.; Cintra, L. T. A.; Duque, C. Cytocompatibility and Synergy of EGCG and Cationic Peptides Against Bacteria Related to Endodontic Infections, in Planktonic and Biofilm Conditions. *Probiotics Antimicrob. Proteins* **2021**, *13* (6), 1808−1819.
(16) Chen, W.; Yang, S.; Li, S.; Lang, J. C.; Mao, C.; Kroll, P.; Tang, L.; Dong, H. Self-Assembled Peptide Nanofibers Display Natural Antimicrobial Peptides to Selectively Kill Bacteria without Compromising Cytocompatibility. *ACS Appl. Mater. Interfaces* **2019**, *11* (32), 28681−28689.
(17) D'souza, A.; Yoon, J. H.; Beaman, H.; Gosavi, P.; Lengyel-Zhand, Z.; Sternisha, A.; Centola, G.; Marshall, L. R.; Wehrman, M. D.; Schultz, K. M.; Monroe, M. B.; Makhlynets, O. V. Nine-Residue Peptide Self-Assembles in the Presence of Silver to Produce a Self-Healing, Cytocompatible, Antimicrobial Hydrogel. *ACS Appl. Mater. Interfaces* **2020**, *12* (14), 17091−17099.
(18) Egli, J.; Siebler, C.; Köhler, M.; Zenobi, R.; Wennemers, H. Hydrophobic Moieties Bestow Fast-Folding and Hyperstability on Collagen Triple Helices. *J. Am. Chem. Soc.* **2019**, *141* (14), 5607−5611.
(19) Singh, A. K. Structure,Synthesis, and Application of Nanoparticles. In *Engineered Nanoparticles*; Elsevier, 2016; pp 19−76. DOI: 10.1016/B978-0-12-801406-6.00002-9.
(20) Mohan, T.; Kleinschek, K. S.; Kargl, R. Polysaccharide Peptide Conjugates: Chemistry, Properties and Applications. *Carbohydr. Polym.* **2022**, *280*, No. 118875.
(21) Roos, E. M. Joint Injury Causes Knee Osteoarthritis in Young Adults. *Curr. Opin. Rheumatol.* **2005**, *17* (2), 195−200.
(22) Gillquist, J.; Messner, K. Anterior Cruciate Ligament Reconstruction and the Long-Term Incidence of Gonarthrosis. *Sports Med.* **1999**, *27* (3), 143−156.
(23) Bullock, J.; Rizvi, S. A. A.; Saleh, A. M.; Ahmed, S. S.; Do, D. P.; Ansari, R. A.; Ahmed, J. Rheumatoid Arthritis: A Brief Overview of the Treatment. *Med. Princ. Pract.* **2019**, *27* (6), 501−507.
(24) Kremer, J. M.; Alarcón, G. S.; Lightfoot, R. W.; Willkens, R. F.; Furst, D. E.; Williams, H. J.; Dent, P. B.; Weinblatt, M. E. Methotrexate for Rheumatoid Arthritis. *Arthritis Rheum.* **1994**, *37* (3), 316−328.
(25) Wang, Q.; Jiang, J.; Chen, W.; Jiang, H.; Zhang, Z.; Sun, X. Targeted Delivery of Low-Dose Dexamethasone Using PCL−PEG Micelles for Effective Treatment of Rheumatoid Arthritis. *J. Controlled Release* **2016**, *230*, 64−72.
(26) Lorscheider, M.; Tsapis, N.; Ur-Rehman, M.; Gaudin, F.; Stolfa, I.; Abreu, S.; Mura, S.; Chaminade, P.; Espeli, M.; Fattal, E. Dexamethasone Palmitate Nanoparticles: An Efficient Treatment for Rheumatoid Arthritis. *J. Controlled Release* **2019**, *296*, 179−189.
(27) Grodzinsky, A. J.; Wang, Y.; Kakar, S.; Vrahas, M. S.; Evans, C. H. Intra-Articular Dexamethasone to Inhibit the Development of Post-Traumatic Osteoarthritis. *J. Orthop. Res.* **2017**, *35* (3), 406−411.
(28) Zhao, Y.; Wei, C.; Chen, X.; Liu, J.; Yu, Q.; Liu, Y.; Liu, J. Drug Delivery System Based on Near-Infrared Light-Responsive Molybdenum Disulfide Nanosheets Controls the High-Efficiency Release of Dexamethasone to Inhibit Inflammation and Treat Osteoarthritis. *ACS Appl. Mater. Interfaces* **2019**, *11* (12), 11587−11601.
(29) Rothenfluh, D. A.; Bermudez, H.; O'Neil, C. P.; Hubbell, J. A. Biofunctional Polymer Nanoparticles for Intra-Articular Targeting and Retention in Cartilage. *Nat. Mater.* **2008**, *7* (3), 248−254.
(30) Hochberg, M. C.; Altman, R. D.; April, K. T.; Benkhalti, M.; Guyatt, G.; McGowan, J.; Towheed, T.; Welch, V.; Wells, G.; Tugwell, P. American College of Rheumatology 2012 Recommendations for the Use of Nonpharmacologic and Pharmacologic Therapies in Osteoarthritis of the Hand, Hip, and Knee. *Arthritis Care Res.* **2012**, *64* (4), 465−474.
(31) Saraf, A.; Mikos, A. G. Gene Delivery Strategies for Cartilage Tissue Engineering. *Adv. Drug Delivery Rev.* **2006**, *58* (4), 592−603.
(32) Huebner, K. D.; Shrive, N. G.; Frank, C. B. Dexamethasone Inhibits Inflammation and Cartilage Damage in a New Model of Post-Traumatic Osteoarthritis. *J. Orthop. Res.* **2014**, *32* (4), 566−572.
(33) Clements, A. E. B.; Murphy, W. L. Injectable Biomaterials for Delivery of Interleukin-1 Receptor Antagonist: Toward Improving Its Therapeutic Effect. *Acta Biomater.* **2019**, *93*, 123−134.
(34) Kavanaugh, T. E.; Werfel, T. A.; Cho, H.; Hasty, K. A.; Duvall, C. L. Particle-Based Technologies for Osteoarthritis Detection and Therapy. *Drug Delivery Transl. Res.* **2016**, *6* (2), 132−147.
(35) Zhu, M.; Wei, K.; Lin, S.; Chen, X.; Wu, C. C.; Li, G.; Bian, L. Bioadhesive Polymersome for Localized and Sustained Drug Delivery at Pathological Sites with Harsh Enzymatic and Fluidic Environment via Supramolecular Host−Guest Complexation. *Small* **2018**, *14* (7), 1702288.
(36) Patel, J. M.; Saleh, K. S.; Burdick, J. A.; Mauck, R. L. Bioactive Factors for Cartilage Repair and Regeneration: Improving Delivery, Retention, and Activity. *Acta Biomater.* **2019**, *93*, 222−238.
(37) Wang, Y.; Katyal, P.; Montclare, J. K. Protein-Engineered Functional Materials. *Adv. Healthc. Mater.* **2019**, *8* (11), 1801374.
(38) Walimbe, T.; Panitch, A. Proteoglycans in Biomedicine: Resurgence of an Underexploited Class of ECM Molecules. *Front. Pharmacol.* **2020**, *10*, 1661 DOI: 10.3389/fphar.2019.01661.
(39) Luo, T.; David, M. A.; Dunshee, L. C.; Scott, R. A.; Urello, M. A.; Price, C.; Kiick, K. L. Thermoresponsive Elastin-b-Collagen-Like Peptide Bioconjugate Nanovesicles for Targeted Drug Delivery to Collagen-Containing Matrices. *Biomacromolecules* **2017**, *18* (8), 2539−2551.
(40) Luo, T.; Kiick, K. L. Noncovalent Modulation of the Inverse Temperature Transition and Self-Assembly of Elastin-b-Collagen-like Peptide Bioconjugates. *J. Am. Chem. Soc.* **2015**, *137* (49), 15362−15365.
(41) Urry, D. W.; Luan, C. H.; Parker, T. M.; Gowda, D. C.; Prasad, K. U.; Reid, M. C.; Safavy, A. Temperature of Polypeptide Inverse Temperature Transition Depends on Mean Residue Hydrophobicity. *J. Am. Chem. Soc.* **1991**, *113* (11), 4346−4348.
(42) Urry, D. W.; Trapane, T. L.; Prasad, K. U. Phase-structure Transitions of the Elastin Polypentapeptide−Water System within the Framework of Composition−Temperature Studies. *Biopolymers* **1985**, *24* (12), 2345−2356.
(43) Urry, D. W.; Gowda, D. C.; Parker, T. M.; Luan, C. -H; Reid, M. C.; Harris, C. M.; Pattanaik, A.; Harris, R. D. Hydrophobicity

Scale for Proteins Based on Inverse Temperature Transitions. *Biopolymers* **1992**, *32* (9), 1243−1250.
(44) Urry, D. W. Physical Chemistry of Biological Free Energy Transduction as Demonstrated by Elastic Protein-Based Polymers. *J. Phys. Chem. B* **1997**, *101* (51), 11007−11028.
(45) Luo, T.; Kiick, K. L. Collagen-Like Peptide Bioconjugates. *Bioconjugate Chem.* **2017**, *28* (3), 816−827.
(46) Dunshee, L. C.; Sullivan, M. O.; Kiick, K. L. Manipulation of the Dually Thermoresponsive Behavior of Peptide-Based Vesicles through Modification of Collagen-like Peptide Domains. *Bioeng. Transl. Med.* **2020**, *5* (1), No. e10145.
(47) Qin, J.; Luo, T.; Kiick, K. L. Self-Assembly of Stable Nanoscale Platelets from Designed Elastin-like Peptide-Collagen-like Peptide Bioconjugates. *Biomacromolecules* **2019**, *20* (4), 1514−1521.
(48) Taylor, P. A.; Huang, H.; Kiick, K. L.; Jayaraman, A. Placement of Tyrosine Residues as a Design Element for Tuning the Phase Transition of Elastin-Peptide-Containing Conjugates: Experiments and Simulations. *Mol. Syst. Des. Eng.* **2020**, *5* (7), 1239−1254.
(49) Hwang, J.; Huang, H.; Sullivan, M. O.; Kiick, K. L. Controlled Delivery of Vancomycin from Collagen-Tethered Peptide Vehicles for the Treatment of Wound Infections. *Mol. Pharmaceutics* **2023**, *20* (3), 1696−1708.
(50) Dunshee, L. C.; McDonough, R. C.; Price, C.; Kiick, K. L. Retention of Peptide-Based Vesicles in Murine Knee Joints after Intra-Articular Injection. *J. Drug Delivery Sci. Technol.* **2022**, *74*, No. 103532.
(51) Li, Y.; Foss, C. A.; Summerfield, D. D.; Doyle, J. J.; Torok, C. M.; Dietz, H. C.; Pomper, M. G.; Yu, S. M. Targeting Collagen Strands by Photo-Triggered Triple-Helix Hybridization. *Proc. Natl. Acad. Sci. U. S. A.* **2012**, *109* (37), 14767−14772.
(52) Prhashanna, A.; Taylor, P. A.; Qin, J.; Kiick, K. L.; Jayaraman, A. Effect of Peptide Sequence on the LCST-Like Transition of Elastin-Like Peptides and Elastin-Like Peptide-Collagen-Like Peptide Conjugates: Simulations and Experiments. *Biomacromolecules* **2019**, *20* (3), 1178−1189.
(53) Doane, T.; Burda, C. Nanoparticle Mediated Non-Covalent Drug Delivery. *Adv. Drug Delivery Rev.* **2013**, *65* (5), 607−621.
(54) Nsairat, H.; Alshaer, W.; Odeh, F.; Esawi, E.; Khater, D.; Bawab, A. Al; El-Tanani, M.; Awidi, A.; Mubarak, M. S. Recent Advances in Using Liposomes for Delivery of Nucleic Acid-Based Therapeutics. *OpenNano* **2023**, *11*, No. 100132.
(55) Boisguérin, P.; Konate, K.; Josse, E.; Vivès, E.; Deshayes, S. Peptide-Based Nanoparticles for Therapeutic Nucleic Acid Delivery. *Biomedicines* **2021**, *9* (5), 583.
(56) Colletier, J. P.; Chaize, B.; Winterhalter, M.; Fournier, D. Protein Encapsulation in Liposomes: Efficiency Depends on Interactions between Protein and Phospholipid Bilayer. *BMC Biotechnol.* **2002**, *2* (1), 9.
(57) Hickey, T.; Kreutzer, D.; Burgess, D. J.; Moussy, F. Dexamethasone/PLGA Microspheres for Continuous Delivery of an Anti-Inflammatory Drug for Implantable Medical Devices. *Biomaterials* **2002**, *23* (7), 1649−1656.
(58) Galeska, I.; Kim, T. K.; Patil, S. D.; Bhardwaj, U.; Chatttopadhyay, D.; Papadimitrakopoulos, F.; Burgess, D. J. Controlled Release of Dexamethasone from PLGA Microspheres Embedded within Polyacid-Containing PVA Hydrogels. *AAPS J.* **2005**, *7* (1), No. E231.
(59) Suyama, K.; Tatsubo, D.; Iwasaki, W.; Miyazaki, M.; Kiyota, Y.; Takahashi, I.; Maeda, I.; Nose, T. Enhancement of Self-Aggregation Properties of Linear Elastin-Derived Short Peptides by Simple Cyclization: Strong Self-Aggregation Properties of Cyclo[FPGVG]n, Consisting Only of Natural Amino Acids. *Biomacromolecules* **2018**, *19* (8), 3201−3211.
(60) Liang, Y.; Kiick, K. L. Liposome-Cross-Linked Hybrid Hydrogels for Glutathione-Triggered Delivery of Multiple Cargo Molecules. *Biomacromolecules* **2016**, *17* (2), 601−614.
(61) Qin, J.; Sloppy, J. D.; Kiick, K. L. Fine Structural Tuning of the Assembly of ECM Peptide Conjugates via Slight Sequence Modifications. *Sci. Adv.* **2020**, *6* (41), 3033−3040.
(62) Kojima, C.; Suehiro, T. Improvement of Temperature-Responsive Drug Release from Collagen-Mimic Dendrimers. *Chem. Lett.* **2011**, *40* (11), 1249−1251.
(63) Nosrati, H.; Adinehvand, R.; Manjili, H. K.; Rostamizadeh, K.; Danafar, H. Synthesis, Characterization, and Kinetic Release Study of Methotrexate Loaded MPEG−PCL Polymersomes for Inhibition of MCF-7 Breast Cancer Cell Line. *Pharm. Dev. Technol.* **2019**, *24* (1), 89−98.
(64) Rainey, K. H.; Patterson, G. H. Photoswitching FRET to Monitor Protein−Protein Interactions. *Proc. Natl. Acad. Sci. U. S. A.* **2019**, *116* (3), 864−873.
(65) Sekar, R. B.; Periasamy, A. Fluorescence Resonance Energy Transfer (FRET) Microscopy Imaging of Live Cell Protein Localizations. *J. Cell Biol.* **2003**, *160* (5), 629−633.
(66) Korsmeyer, R. W.; Peppas, N. A. Effect of the Morphology of Hydrophilic Polymeric Matrices on the Diffusion and Release of Water Soluble Drugs. *J. Membr. Sci.* **1981**, *9* (3), 211−227.
(67) Ciobanu, A. M.; Bârcă, M.; Manda, G.; Dragomiroiu, G. T. A. B.; Baconi, D. L. Methotrexate Liposomes - A Reliable Therapeutic Option. In *Liposomes*; Catala, A., Ed.; InTech: Rijeka, 2017; p Ch. 10. DOI: 10.5772/intechopen.68520.
(68) Mesquita, P. C.; Oliveira, A. R.; Pedrosa, M. F. F.; de Oliveira, A. G.; da Silva-Júnior, A. A. Physicochemical Aspects Involved in Methotrexate Release Kinetics from Biodegradable Spray-Dried Chitosan Microparticles. *J. Phys. Chem. Solids* **2015**, *81*, 27−33.
(69) Calapoglu, F.; Sahin, S.; Ozmen, I.; Ozbek Yazici, S. Investigation of Interaction between Dexamethasone/Pheniramine and Trypsin by Fluorescence, UV-Vis, CD, and Molecular Docking. *J. Biomol. Struct. Dyn.* **2023**, *41* (6), 2202−2210.
(70) Gu, X.; Qiu, M.; Sun, H.; Zhang, J.; Cheng, L.; Deng, C.; Zhong, Z. Polytyrosine Nanoparticles Enable Ultra-High Loading of Doxorubicin and Rapid Enzyme-Responsive Drug Release. *Biomater. Sci.* **2018**, *6* (6), 1526−1534.
(71) Guo, Y.; Zhao, S.; Qiu, H.; Wang, T.; Zhao, Y.; Han, M.; Dong, Z.; Wang, X. Shape of Nanoparticles as a Design Parameter to Improve Docetaxel Antitumor Efficacy. *Bioconjugate Chem.* **2018**, *29* (4), 1302−1311.
(72) Lim, C.; Ramsey, J. D.; Hwang, D.; Teixeira, S. C. M.; Poon, C.; Strauss, J. D.; Rosen, E. P.; Sokolsky-Papkov, M.; Kabanov, A. V. Drug-Dependent Morphological Transitions in Spherical and Worm-Like Polymeric Micelles Define Stability and Pharmacological Performance of Micellar Drugs. *Small* **2022**, *18* (4), 2103552.
(73) Guo, F.; Ouyang, T.; Peng, T.; Zhang, X.; Xie, B.; Yang, X.; Liang, D.; Zhong, H. Enhanced Oral Absorption of Insulin Using Colon-Specific Nanoparticles Co-Modified with Amphiphilic Chitosan Derivatives and Cell-Penetrating Peptides. *Biomater. Sci.* **2019**, *7* (4), 1493−1506.
(74) Hou, M.; Gao, Y.-E.; Shi, X.; Bai, S.; Ma, X.; Li, B.; Xiao, B.; Xue, P.; Kang, Y.; Xu, Z. Methotrexate-Based Amphiphilic Prodrug Nanoaggregates for Co-Administration of Multiple Therapeutics and Synergistic Cancer Therapy. *Acta Biomater.* **2018**, *77*, 228−239.
(75) Narayani, R.; Panduranga Rao, K. Collagen-Poly (HEMA) Hydrogels for the Controlled Delivery of Methotrexate and Cisplatin. *Int. J. Pharm.* **1996**, *138* (1), 121−124.
(76) Krzeski, P.; Buckland-Wright, C.; Bálint, G.; Cline, G. A.; Stoner, K.; Lyon, R.; Beary, J.; Aronstein, W. S.; Spector, T. D. Development of Musculoskeletal Toxicity without Clear Benefit after Administration of PG-116800, a Matrix Metalloproteinase Inhibitor, to Patients with Knee Osteoarthritis: A Randomized, 12-Month, Double-Blind, Placebo-Controlled Study. *Arthritis Res. Ther.* **2007**, *9* (5), R109.
(77) Despanie, J.; Dhandhukia, J. P.; Hamm-Alvarez, S. F.; MacKay, J. A. Elastin-like Polypeptides: Therapeutic Applications for an Emerging Class of Nanomedicines. *J. Controlled Release* **2016**, *240*, 93−108.
(78) Parmar, P. A.; Chow, L. W.; St-Pierre, J.-P.; Horejs, C.-M.; Peng, Y. Y.; Werkmeister, J. A.; Ramshaw, J. A. M.; Stevens, M. M. Collagen-Mimetic Peptide-Modifiable Hydrogels for Articular Cartilage Regeneration. *Biomaterials* **2015**, *54*, 213−225.

(79) Arlotta, K. J.; San, B. H.; Mu, H. H.; Yu, S. M.; Owen, S. C. Localization of Therapeutic Fab-CHP Conjugates to Sites of Denatured Collagen for the Treatment of Rheumatoid Arthritis. *Bioconjugate Chem.* **2020**, *31* (8), 1960−1970.
(80) Zitnay, J. L.; Li, Y.; Qin, Z.; San, B. H.; Depalle, B.; Reese, S. P.; Buehler, M. J.; Yu, S. M.; Weiss, J. A. Molecular Level Detection and Localization of Mechanical Damage in Collagen Enabled by Collagen Hybridizing Peptides. *Nat. Commun.* **2017**, *8* (1), 14913.



https://doi.org/10.1021/acs.biomac.3c01361
*Biomacromolecules* 2024, 25, 2408−2422